

AD _____

GRANT NUMBER DAMD17-94-J-4292

TITLE: Improved Mammographic Technique for Breast Cancer Diagnosis

PRINCIPAL INVESTIGATOR: Heang-Ping Chan, Ph.D.

CONTRACTING ORGANIZATION: University of Michigan
Ann Arbor, Michigan 48109-1274

REPORT DATE: August 1998

TYPE OF REPORT: Annual

PREPARED FOR: Commander
U.S. Army Medical Research and Materiel Command
Fort Detrick, Maryland 21702-5012

DISTRIBUTION STATEMENT: Approved for Public Release;
Distribution Unlimited

The views, opinions and/or findings contained in this report are those of the author(s) and should not be construed as an official Department of the Army position, policy or decision unless so designated by other documentation.

REPORT DOCUMENTATION PAGE

*Form Approved
OMB No. 0704-0188*

Public reporting burden for this collection of information is estimated to average 1 hour per response, including the time for reviewing instructions, searching existing data sources, gathering and maintaining the data needed, and completing and reviewing the collection of information. Send comments regarding this burden estimate or any other aspect of this collection of information, including suggestions for reducing this burden, to Washington Headquarters Services, Directorate for Information Operations and Reports, 1215 Jefferson Davis Highway, Suite 1204, Arlington, VA 22202-4302, and to the Office of Management and Budget, Paperwork Reduction Project (0704-0188), Washington, DC 20503.

1. AGENCY USE ONLY <i>(Leave blank)</i>			2. REPORT DATE August 1998		3. REPORT TYPE AND DATES COVERED Annual (11 Jul 97 - 10 Jul 98)		
4. TITLE AND SUBTITLE Improved Mammographic Technique for Breast Cancer Diagnosis			5. FUNDING NUMBERS DAMD17-94-J-4292				
6. AUTHOR(S) Heang-Ping Chan, Ph.D.							
7. PERFORMING ORGANIZATION NAME(S) AND ADDRESS(ES) University of Michigan Ann Arbor, Michigan 48109-1274			8. PERFORMING ORGANIZATION REPORT NUMBER				
9. SPONSORING / MONITORING AGENCY NAME(S) AND ADDRESS(ES) U.S. Army Medical Research and Materiel Command Fort Detrick, Maryland 21702-5012			10. SPONSORING / MONITORING AGENCY REPORT NUMBER				
11. SUPPLEMENTARY NOTES							
12a. DISTRIBUTION / AVAILABILITY STATEMENT Approved for Public Release; Distribution Unlimited				12b. DISTRIBUTION CODE			
DTIC QUALITY INSPECTED 4				1 9 9 9 0 2 1 9 1 0 7			
13. ABSTRACT <i>(Maximum 200 words)</i>							
<p>During the fourth year of the project, we have (a) completed a simulation study of the effects of equalization and filter misalignment, (b) designed and built a prototype compressible tank for equalization with a prone mammography system, (c) studied the dynamic range and contrast for equalization using the new liquid bolus method, and (d) studied the optimization of mammographic imaging techniques by Monte Carlo modeling. We have demonstrated the feasibility of the original approach of constructing a near-patient specific external filter device for x-ray equalization. We have also investigated the design and construction of a prototype compressible tank for the new approach. We have identified some potential tissue-equivalent liquids that can be used for equalization with the immersion method. The new approach is a significant step towards the practical implementation of the x-ray equalization technique. The optimal techniques and detectors for mammographic imaging without the dynamic range limitation by the detector are being studied by Monte Carlo modeling. In the no-cost-time-extension year, we plan to continue the investigation of the new equalization technique and the optimization of the mammographic imaging system..</p>							
14. SUBJECT TERMS Breast Cancer Mammography, exposure equalization, dynamic range compression, breast cancer detection					15. NUMBER OF PAGES 74		
					16. PRICE CODE		
17. SECURITY CLASSIFICATION OF REPORT Unclassified		18. SECURITY CLASSIFICATION OF THIS PAGE Unclassified		19. SECURITY CLASSIFICATION OF ABSTRACT Unclassified		20. LIMITATION OF ABSTRACT Unlimited	

FOREWORD

Opinions, interpretations, conclusions and recommendations are those of the author and are not necessarily endorsed by the U.S. Army.

Where copyrighted material is quoted, permission has been obtained to use such material.

Where material from documents designated for limited distribution is quoted, permission has been obtained to use the material.

HPC Citations of commercial organizations and trade names in this report do not constitute an official Department of Army endorsement or approval of the products or services of these organizations.

In conducting research using animals, the investigator(s) adhered to the "Guide for the Care and Use of Laboratory Animals," prepared by the Committee on Care and use of Laboratory Animals of the Institute of Laboratory Resources, national Research Council (NIH Publication No. 86-23, Revised 1985).

HPC For the protection of human subjects, the investigator(s) adhered to policies of applicable Federal Law 45 CFR 46.

In conducting research utilizing recombinant DNA technology, the investigator(s) adhered to current guidelines promulgated by the National Institutes of Health.

In the conduct of research utilizing recombinant DNA, the investigator(s) adhered to the NIH Guidelines for Research Involving Recombinant DNA Molecules.

In the conduct of research involving hazardous organisms, the investigator(s) adhered to the CDC-NIH Guide for Biosafety in Microbiological and Biomedical Laboratories.

ChanDeang Png
PI - Signature

8/6/98
Date

(4) Table of Contents

(1)	Front Cover	1
(2)	Standard Form (SF) 298, REPORT DOCUMENTATION PAGE.....	2
(3)	FOREWORD	3
(4)	Table of Contents	4
(5)	Introduction	5
(6)	Body	7
	(A) Simulation Study of Effects of Equalization and Filter Misalignment.....	7
	(B) Development of a Prototype Compressible Tank for Equalization with a Prone Mammography System	8
	(C) Dynamic Range and Contrast Study for Equalization using a Liquid Bolus	9
	(D) Monte Carlo Modeling of Mammographic Imaging System	12
	(E) Illustrations	14
(7)	Conclusions	18
(8)	References	19
(9)	Appendix	21

(5) Introduction

Breast cancer is one of the leading causes of death among women. There is considerable evidence that early diagnosis and treatment significantly improve the chance of survival for patients with breast cancer [Baker 1982]. At present, x-ray mammography is the only diagnostic procedure with a proven capability for detecting early-stage, clinically occult breast cancers [Baker 1982]. Although mammography has a high sensitivity for detection of breast cancer when compared to other diagnostic procedures, studies indicate that radiologists identify only 70 to 90% of the lesions present [Haug 1987; Baines 1986]. The miss rate is particularly high in dense breasts [D'Agincourt 1993; Wallis 1991].

One of the difficulties in interpretation of mammograms by radiologists is caused by the limited latitude and contrast sensitivity of mammographic screen/film systems. Mammographic abnormalities related to early breast cancers include clustered microcalcifications, spiculated and irregular masses, areas of parenchymal distortion, and skin thickening [Sickles 1986]. These abnormalities are often subtle and low contrast. Therefore, low energy radiation and high contrast screen/film systems are recommended for mammographic imaging in order to increase the contrast between the lesion and the background tissue. Despite the use of vigorous compression during examinations, the low-energy x-ray beam results in a wide dynamic range (the ratio of the maximum to the minimum x-ray exposure at the detector) for the radiation penetrating the breast. This range can be greater than 100. On the other hand, high-contrast film provides a narrow latitude which is about 10 for a typical mammographic system [Bunch 1987]. As a result, thick and glandular regions of the breast are often imaged at the toe of the sigmoid-shaped sensitometric curve of the screen/film system; whereas thin peripheral regions are imaged at the shoulder. The contrast and signal-to-noise ratio (SNR) of mammographic features are greatly reduced in these regions due to decreased film gradient and increased noise. The contrast sensitivity of the human visual system also drops rapidly as the film density increases [Baxter 1982; Snyder 1985]. Kopans [D'Agincourt 1993] found that 70% of breast cancers in women with dense breasts are in the periphery of the mammary parenchyma adjacent to the subcutaneous fat or retromammary fat. The poor image quality in the peripheral region thus imposes a serious limitation on the sensitivity of cancer detection in breasts with dense fibroglandular tissue.

We proposed a practical and cost-effective exposure equalization method for reducing the dynamic range of the x-ray image. The shapes of compressed breasts of the patient population will be analyzed and classified into a finite number of groups. A shaped filter for attenuating x-rays in the peripheral region of the breasts will be fabricated for each group. For a given patient, the breast shape during compression will be classified into one of these groups and the filter for the selected group will be used for this patient. With this technique, the dynamic range of the x-ray intensities incident on the recording system will be reduced and the entire image can be recorded in the high contrast region of the film. The improved image quality can be achieved without additional radiation dose to the patient. Furthermore, a very high-contrast mammographic technique may be developed in combination with exposure equalization to further improve the signal-to-noise ratio (SNR) of the subtle lesions. We expect that the optimized technique will significantly improve the detectability of cancers in mixed and dense breasts and increase the efficacy of mammography as a screening and diagnostic tool for breast cancers.

In the course of the research, we have designed a new approach to the implementation of an x-ray equalization filter for mammography, as we mentioned in last year's report. In this new

approach, the patient breast will be immersed in a compressible tank containing a tissue-equivalent fluid that is compressed together with the breast during x-ray exposure. The fluid will fill any space between the breast, the cassette holder and the compression paddle. Therefore, the filter is truly patient specific and tissue-equivalent.

During this year, we have completed the simulation study of the effects of equalization and filter misalignment. We have further investigated possible tissue-equivalent liquids and built a prototype of the compressible tank. A Monte Carlo simulation study for optimization of the mammographic imaging technique has also been performed. Detailed description is included in the Body of this report.

(6) Body

In the fourth year (7/11/97-7/10/98) of this grant, we have performed the following studies:

(A) Simulation Study of Effects of Equalization and Filter Misalignment

We have completed the simulation study of the effects of equalization and filter alignment and have submitted a manuscript to the Medical Physics journal for consideration of publication. A copy of the manuscript is enclosed with this progress report. The results of the study were detailed in the manuscript. Some of the important findings are summarized below.

Better simulated equalization filters were designed by disregarding sections in the digitized mammograms where there were significant artifacts due to nonuniform response and blooming artifacts (saturation tails) associated with our CCD film digitizer. Examples of the original mammograms and the improved equalized mammograms that were obtained in our latest simulation studies are shown in Figure 1.

The effectiveness of the filters were evaluated the filter effectiveness on 171 mediolateral and 196 craniocaudal view digitized mammograms. The breast shape of each image was automatically detected and the set of images in each view was classified into groups of similar shape. The largest group of each view was selected for the simulation study. A filter was designed for each group as described in the last report. The filter was then automatically aligned with each breast and the imaging process with the filter in the x-ray beam was simulated. The "equalized" images were evaluated visually by an experienced radiologist for misalignment artifacts. The degree of match between the filter and the individual 3-D exposure profiles at the breast periphery was quantified with a figure-of-merit (FoM) that was computed from data along normals to the detected breast boundary in the unfiltered images. The normals consisted of 31 pixels, 10 outside and 20 inside the breast area in the image. A correlation coefficient between the filter profile and the pixel values in the unfiltered image along the normal to the breast boundary was first calculated using the equation

$$corf(i) = \frac{\sum_j (pix(i,j) - mpix(i)) (pixcor(i,j) - mpixcor(i))}{\left[\sum_j (pix(i,j) - mpix(i))^2 \right]^{1/2} \left[\sum_j (pixcor(i,j) - mpixcor(i))^2 \right]^{1/2}}$$

where $pix(i,j)$ and $mpix(i)$ indicate the j th pixel value and the mean pixel value along the i th normal in an unfiltered image. The values $pixcor(i,j)$ and $mpixcor(i)$ are the transformed pixel value increment and the mean transformed pixel value increment, respectively, along the same i th normal. The summation j was over all 31 points along the i th normal.

The correlation coefficients for all the normals in a given image were averaged and a mean correlation coefficient was obtained. This mean correlation coefficient was used as the FoM that quantified the match between the filter and the breast image. An FoM value of 1.0

indicated perfect match and 0 indicated no match. The distributions of the FoM for the group of CC-view and MLO-view images are shown in Figure 2.

We performed a misalignment analysis to investigate the effect of mismatch. For a given image, the filter was displaced laterally and transversely in 2 mm increments in the four directions away from the automatically aligned location. The imaging process through the filter was simulated at each displaced location. The "equalized" image was evaluated both visually and by the FoM. One example of the misalignment study is shown in Figure 3. It was estimated that the tolerance for misalignment on the image plane would be up to 2 mm for CC view and 1 mm for MLO-view without disturbing artifacts on the images. When the filter is placed near the collimator, the tolerance of alignment at the filter plane will be about 0.3 mm. Such a tolerance is achievable through commercially available x-y translators.

In summary, our simulation study indicates the effectiveness of an exposure equalization technique for mammographic imaging using a small set of near patient-specific external filters. The visibility of image details in the peripheral region of the breast is improved by equalization. It is shown that an average filter for a group of breasts with a similar shape can be designed using a polynomial to represent the breast shape and an average exposure profile to derive the thickness distribution. This average filter can provide exposure equalization without significant misalignment artifacts for approximately 80% of the images used in this study. It is feasible to build a computerized external filter device to automatically select the appropriate filter and align the chosen filter with the breast. Some artifacts can occur due to large misalignments in the filter position. The effects of equalization were also studied by phantom experiments using prototype filters.

(B) Development of a Prototype Compressible Tank for Equalization with a Prone Mammography System

Last year we proposed a new technique that promises to be practical and will produce superior images. Our new approach is to image the breast in a prone mammographic x-ray system. The breast will be immersed in a tissue-equivalent liquid in a compressible tank installed under the table. The liquid will be compressed together with the breast during x-ray exposure. The tissue-equivalent filter will therefore fit breasts of any thickness or any shape, and will work imaged in any mammographic view. It will provide a truly patient-specific, tissue-equivalent filter around the patient's breast to reduce the x-ray intensity.

The key step of this approach is the design of a compressible tank. With the approval from the USAMRMC, we purchased a Fischer biopsy table which is a prone mammography system. We worked with a group of mechanical engineering student at the University of Michigan to design and build a prototype compressible tank. A prototype tank was built which is shown in Figure 4. It was designed with the following features

- (1) The tank is a self-supporting structure to be added on a prone mammography system. It can be rotated with the x-ray tube supporting arm to any angle for different mammographic views.
- (2) The tank is U-shaped with a front wall that can be moved in or out of the tank by a motorized control arm. The front wall serves as a paddle which can exert up to 40 lb

pressure to compress the breast. The paddle has a rectangular window made with a thin plastic material for high x-ray transmission. The x-ray attenuation of the plastic material was found to be negligible. The paddle is fitted with a rubber seal around the edges to prevent leakage.

- (3) The tank is equipped with a fluid handling subsystem for filling and emptying the tank with tissue-equivalent fluid and cleaning chemicals.
- (4) The tank has a drainage system to prevent overflow. Overflow will occur because the fluid has to be filled to the chest wall level which is also the top of the tank.

After testing the prototype, we found that there are some problems in the current design. First, the friction between the rubber seal and the tank is too large and the paddle has to be lubricated. The lubricant can contaminate the fluid in the tank. Second, there are grooves on the paddle which are difficult to clean and sterilize if the tank is used for patients. Third, the fluid filling system generates bubbles in the tank which may create artifacts on the mammogram. We will continue to improve the design to reduce these problems and perform phantom studies to verify its performance.

(C) Dynamic Range and Contrast Study for Equalization using a Liquid Bolus

A key advantage of the liquid bolus exposure equalization method that we are proposing is that it results in patient specific exposure reduction at the breast periphery. The consequent equalization of the detected x-ray exposures at the center and periphery of the breast is especially useful for screen-film detectors, which are characterized by a non-linear response that results in reduced contrast at high and low exposures. It is also useful for digital detectors because it facilitates the acquisition of the entire image at an optimal signal to noise ratio which cannot be accomplished with postprocessing techniques such as those proposed by Byng et al [Byng 1997] and Bick et al [Bick 1996]. As demonstrated by Lam and Chan [Lam 1990] the liquid medium will reduce the amount of scattered radiation striking the detector at the peripheral region, which should improve image contrast. However, any external beam equalization filter including a liquid bolus will increase the x-ray beam hardening in the peripheral region, which will reduce image contrast. Hence there can be a tradeoff between the desired reduction in dynamic range and the undesired possible reduction in image contrast. The amount of dynamic range and contrast reduction will depend upon the x-ray attenuation properties of the particular liquid that is employed.

In order to determine which liquid would be best for this application, we performed a simulation study in which we quantified the effects of various liquid bolus materials on dynamic range and image contrast. In this simulation, we employed the measured mammography spectra of Jennings and Fewell [Jennings] and the elemental compositions of glandular and adipose tissues of Hammerstein, et al.[Hammerstein 1979] Mass attenuation coefficients for the tissues, calcification, bolus liquids and detectors were computed with the XCOM computer program of Berger and Hubbell of the National Bureau of Standards. The energy absorption coefficients of the detectors were computed from Storm and Israel's tables [Storm 1970]. Two of the detectors that were modeled were a minR screen and an amorphous selenium plate. The minR screen is made of $\text{Gd}_2\text{O}_2\text{S:Tb}$ and has an areal density of 33.7 mg/cm^2 and a thickness of 100 microns. [Bunch] The amorphous selenium (a-Se) plate was assumed to be 200 microns [Zhao 1997] thick and had a density of 4.27 g/cc [Fahrig 1996]. K-reabsorption in the Selenium detector (K-edge = 12.658 keV) was included in our calculations [Chan 1983]; it was not used for the minR screen because the maximum energy spectrum employed (36 kVp) was below the K-edge of Gd (50.239 keV). Both the dynamic range and contrast were computed for total breast thicknesses

of 3, 5, and 8 cm. The contrast was computed near the periphery of the breast for a 100-micron thick microcalcification made of calcium hydroxyapatite in a 1-cm thick section of average breast tissue (50% adipose/50% glandular). Molybdenum target spectra filtered with 30 microns of Molybdenum were assumed for all breast thicknesses. Although a higher atomic number filter would probably be employed when imaging an 8-cm breast, the calculation provides a worst case assessment of dynamic range requirements.

The dynamic range is the ratio the maximum energy absorbed in the detector to the minimum. For conventional imaging, the dynamic range is computed as the ratio of the energy absorbed in the detector in the air region adjacent to the breast to the energy absorbed in the detector beneath pure glandular tissue that extends throughout the entire breast thickness. When a liquid bolus is adjacent to the breast, the maximum energy absorbed is either beneath the bolus or beneath pure adipose tissue, whichever is less attenuating. Contrast was computed as the ratio $(Eabs_1 - Eabs_2)/Eabs_1$ where $Eabs_1$ is the absorption in the detector under a 1 cm thick breast tissue region without the microcalcification and $Eabs_2$ is the absorption in the same region with the 100 micron microcalcification.

Results are listed in the tables below. According to Fahrig, Rolands and Yaffee [Fahrig 1996], "the optimal spectral conditions (for a-Se and digital systems based on Gd_2O_2S) are essentially identical to those determined empirically for conventional screen-film systems." Therefore the following comparisons were made using spectra similar to those employed in the clinic (26 kVp for 3 cm, 28 kVp for 5 cm, and 30 kVp for 8 cm).

Table 1: Dynamic Range: Maximum energy absorbed/ Minimum energy absorbed in detector. (materials for max/min are given in parentheses)

Condition	Detector	No bolus (air/gland)	Fat bolus (fat/gland)	Adipose bolus (Adip./gland)	50%water/ 50%fat bolus (Adip./gland)	Water bolus (adip./water)
26 kVp, 3 cm	Gd_2O_2S : a-Se:	29.1 25.8	4.3 4.1	3.2 3.0	3.2 3.0	3.3 3.2
28 kVp, 5 cm	Gd_2O_2S : a-Se:	144.6 115.4	7.6 6.8	4.9 4.5	4.9 4.5	5.2 4.7
30 kVp, 8 cm	Gd_2O_2S : a-Se:	817.1 544.3	10.8 8.7	6.2 5.2	6.2 5.2	6.3 5.3

Table 2. Primary Contrast (1 cm breast tissue with 100 micron calcification)

Bolus Material							
Condition	Bolus Thickness*	Detector	None (air)	fat	adipose	50%water/ 50%fat	water
26 kVp	2 cm	Gd_2O_2S : a-Se:	28.3% 27.3%	25.8% 25.0%	25.4% 24.6%	24.8% 24.0%	23.8% 23.0%
28 kVp	4 cm	Gd_2O_2S : a-Se:	27.3% 26.2%	23.2% 22.1%	22.4% 21.3%	21.3% 20.1%	19.3% 18.1%
30 kVp	7 cm	Gd_2O_2S : a-Se:	26.5% 25.2%	19.5% 17.9%	17.9% 16.4%	15.7% 14.4%	12.8% 11.9%

* Total breast thickness = bolus thickness + 1 cm
(contrast computed with bolus above and below the 1-cm tissue segment studied)

The data in Tables 1 and 2 indicate that the use of bolus materials such as fat and adipose tissue will reduce the dynamic range requirements for detection and display while producing mild

to moderate reduction in contrast due to beam hardening. So long as the detector has sufficient signal to noise ratio, much of the latter can be compensated for by employing an increased slope in the contrast transfer curve for display. Also, the overall image contrast will be improved when a bolus material is employed because less scattered radiation will be detected near the periphery of the breast.[Lam 1990] Much of this scatter arises from the breast surface, and when a bolus material is not employed, the tissue thickness is thinner near the periphery, absorbing less scatter. Finally, it is interesting to note that more attenuation liquids such as water and a 50% water/50% fat emulsion that simulates average breast tissue are also effective at reducing the dynamic range. However they do so at the penalty of significantly reducing image contrast, especially for larger breasts.

Based on this study, vegetable oils, which are 100% fat, would be close to ideal exposure equalization media. The primary disadvantage of these oils is that they are greasy and messy, and would be difficult to clean out from the breast immersion/compression tank between patient studies. During the 1-year extension period for this project, we will investigate other liquid candidates. This investigation will include performing a study to determine the least concentration of water that might be employed to produce a stable fat-in-water emulsion medium for exposure equalization. We have obtained samples of a 50% fat-50% water emulsion that is commercially available (MicroLipid from Mead Johnson, Inc.). This emulsion has the consistency of milk, which would be much more acceptable for patient studies. It is anticipated that higher concentrations of oil will make the emulsion greasier, and a compromise concentration may need to be determined. Other liquids including adipose tissue substitutes such as ethylene glycol monoethyl ether ($C_4H_{10}O_2$) and a solution of water, urea, propanol and phosphoric acid that have been suggested by White and Constantinou [White 1982] will also be investigated. In addition to the requirements that the liquids yield acceptable dynamic range and contrast reductions and be easy to clean from the tank, we will also require that the liquids not be "carcinogenic, corrosive, toxic, explosive, volatile, deliquescent, or unpleasant to use." [Constantinou 1982] Furthermore, the liquids "must not undergo internal reaction or absorb CO_2 from the air", and they "must be stable to radiation with time, inert, and commercially available and moderate in cost." [Constantinou 1982]

The dynamic range and contrast for each liquid candidate will be computed using the techniques described above for our previous investigation. The elemental compositions and mass densities of the liquids will be needed for the computations. Both should in most cases be available in reference books. If not, they will be measured.

Experimental studies will also be performed in which breast-simulating phantoms of various thicknesses and adipose/glandular compositions will be imaged while immersed in the liquids. Each phantom will contain clusters of microcalcifications and simulated masses in the peripheral and middle regions. Custom phantoms will be designed and manufactured for this purpose. They will more closely simulate breasts, in particular the glandular and adipose tissue distribution, than most of the phantoms that are presently commercially available. Imaging of the phantoms will be performed on the Fischer prone mammography system that was purchased for this project. The breast immersion tank that was designed and built by a group of University of Michigan Mechanical Engineering students under our guidance will be employed. The image receptor will be a high-resolution 8" x 10" computed radiography (CR) plate. These plates are employed in our clinical Siemens/Fuji CR system. The amplitude histogram facilities of the

image workstation in this system will be used to assess the dynamic range and contrasts for the various phantom/liquid combinations studied. The experimental values will be compared with those computed analytically. Reasons for any discrepancies in these results will be investigated.

(D) Monte Carlo Modeling of Mammographic Imaging System

As a continuation of the Monte Carlo study described in last year's progress report, we performed a simulation study to evaluate various x-ray detectors for digital mammography. We used the MCNP Monte Carlo code from Los Alamos National laboratory. The image contrast and noise properties of the detectors were evaluated for the task of imaging a 200 micron microcalcification in a 5-cm-thick breast of average 50% adipose/50% glandular tissue composition. The entire imaging process was simulated including the use of a mammography imaging geometry, measured x-ray spectra from a Mo target, Mo filter x-ray tube [Jennings] at x-ray tube potentials ranging from 24 kVp to 38 kVp, and a moving grid with a 5:1 grid ratio and grid frequency of 31 lines/cm. Primary contrast was computed analytically and included reabsorption of K-characteristic x-rays in the detector. Scatter fraction both with and without the grid were computed with the Monte Carlo simulation. The quantum noise and mean glandular dose were also computed with the Monte Carlo simulation. The detector MTF was not included in the model nor were sources of noise other than quantum. The detectors that were studied are listed in Table 3 below. They included both direct detectors (e.g. a-Se, CdZnTe, and PbI₂) and indirect detectors (screens such as CsI and Gd₂O₃S backed by flat panel active matrix detectors).

Table 3. Detector materials studied with Monte Carlo modeling of a mammographic imaging system.

Detector	Thickness (μm)	Density (g/cm ³)
Gd ₂ O ₃ S	100	3.38
CsI	100	4.50
a-Se	200	4.27
PbI ₂	100	5.00
CdZnTe	100	5.50

Test cases were also simulated to verify the accuracy of our model. We found that the mean glandular doses computed with our model were within 1 to 4% of those computed by Wu et al. [Wu 1991]. The scatter fractions were within 10% of those we measured experimentally and those measured by Rezentes et al [Rezentes 1998]. Finally, the primary contrasts were within 4% of those computed by Dance et al [Dance 1992].

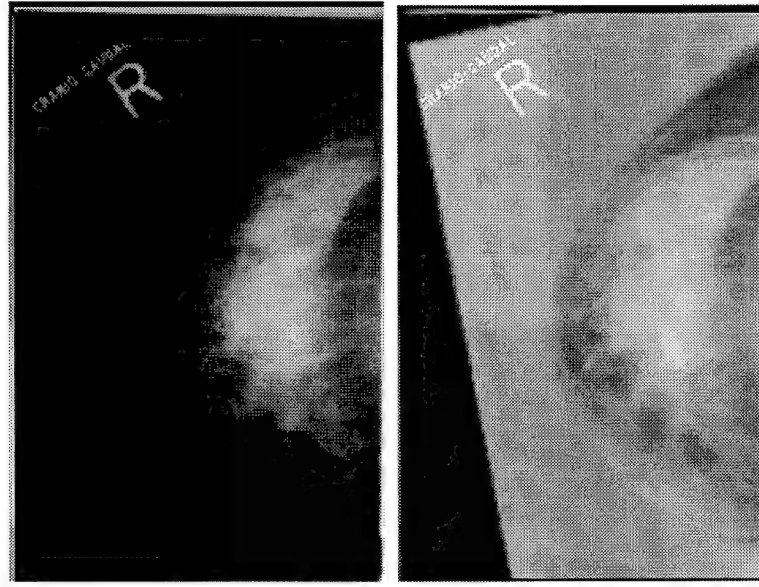
A figure of merit (FoM) was derived to compare the detectors. This FoM was the ratio of the square of the contrast-to-noise-ratio (CNR) divided by the mean glandular dose. Plots of the FoM's for the various indirect detectors at the various kVp's when a grid is employed are shown in Figure 5. Corresponding plots for the direct detectors are shown in Figure 6. Results for the no-grid condition are shown in Figures 7 and 8.

From the above plots, the maximum FoM occurs between 28 and 30 kVp, regardless of the detector. This is true both with and without the grid. For the particular detector thicknesses studied, and only considering quantum noise, the ranking of the detectors from best to worst

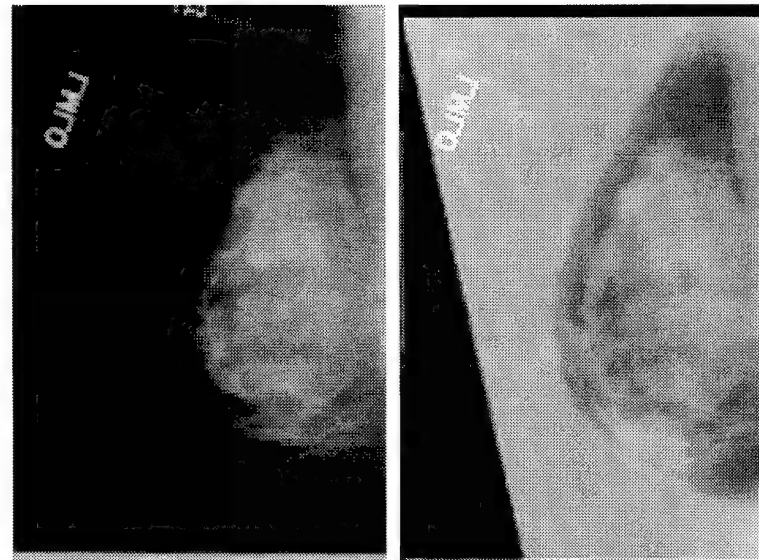
according to their FoM's is: $\text{Gd}_2\text{O}_3\text{S}$, PbI_2 , a-Se, CdZnTe, and CsI. It is expected that this ranking will depend on the thickness of the detector material.

Future studies will be carried out using different detector thicknesses, different spectra, in particular, harder (higher effective energy) spectra from a tungsten target and from a Mo target with a Rhodium filter. The FoM's for the harder spectra are expected to be better since the dose for such spectra will be less, and the CNR will not degrade too much so long as the energy is not too great. Also, the FoM's will be computed for a simulated microcalcification in breasts of different thicknesses and compositions. The optimal energy is expected to change with breast thickness. These studies will provide guidance for spectrum selection when imaging breasts of various thicknesses and compositions with the different digital detectors.

(D) Illustrations

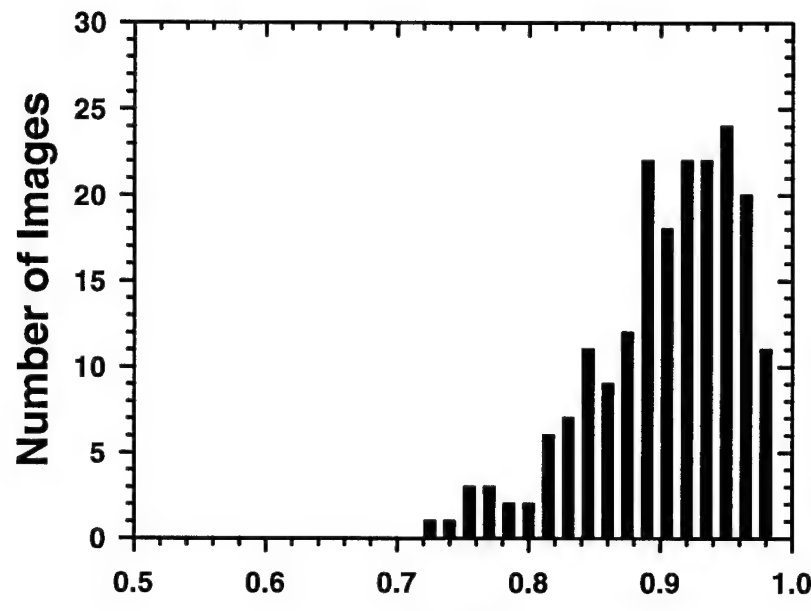


(a)

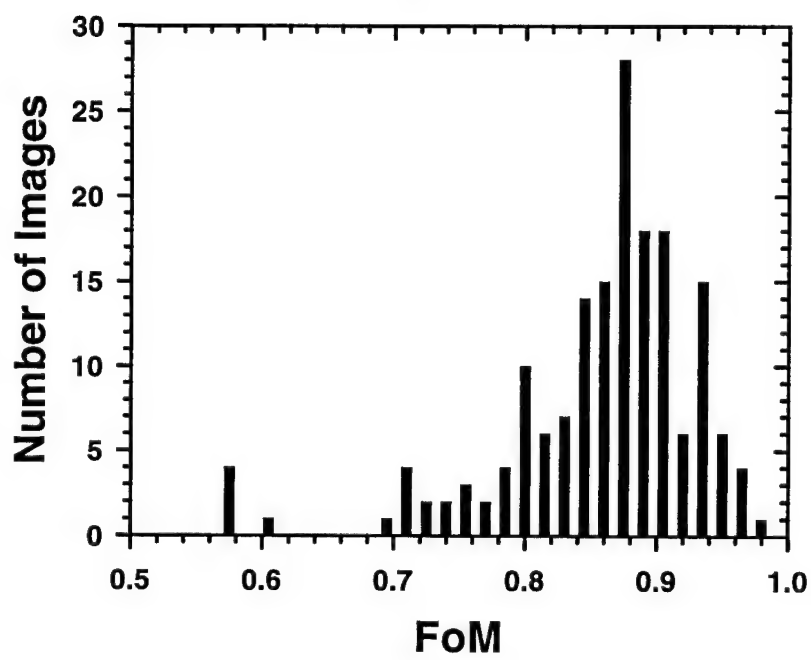


(b)

Figure 1. Examples of (a) unequalized and equalized CC-view images, (b) unequalized and equalized MLO-view images.



(a)



(b)

Figure 2. Distribution of the Figure-of-Merit for the group of (a) CC-view and (b) MLO view images.

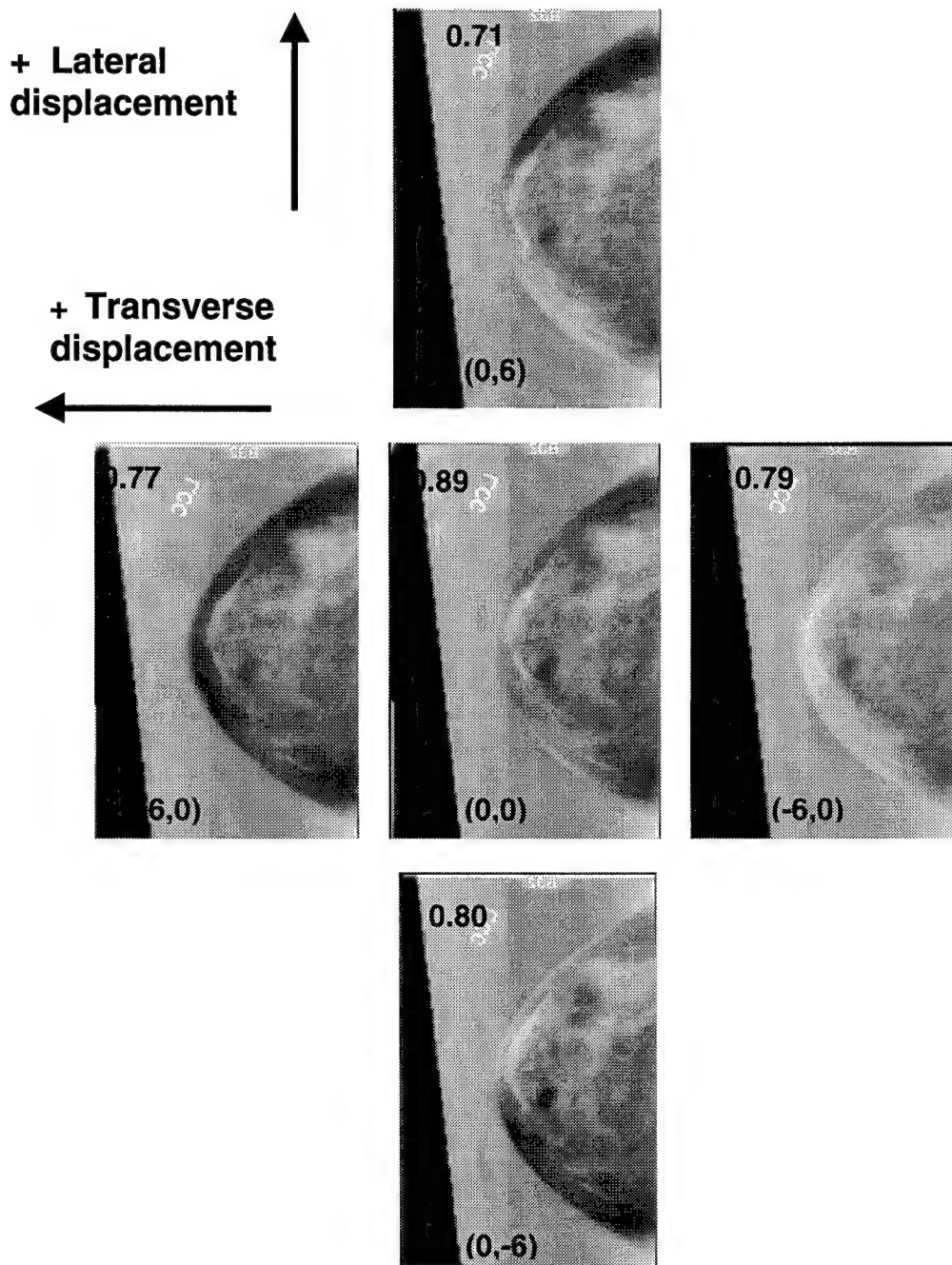


Figure 3. Effect of filter misalignment on the FoM. The dark areas seen along the breast periphery are due to under-compensation whereas the lighter areas are due to over-compensation. The numbers in parentheses indicate the filter displacements and the numbers at the upper left corner are the corresponding FoM values.

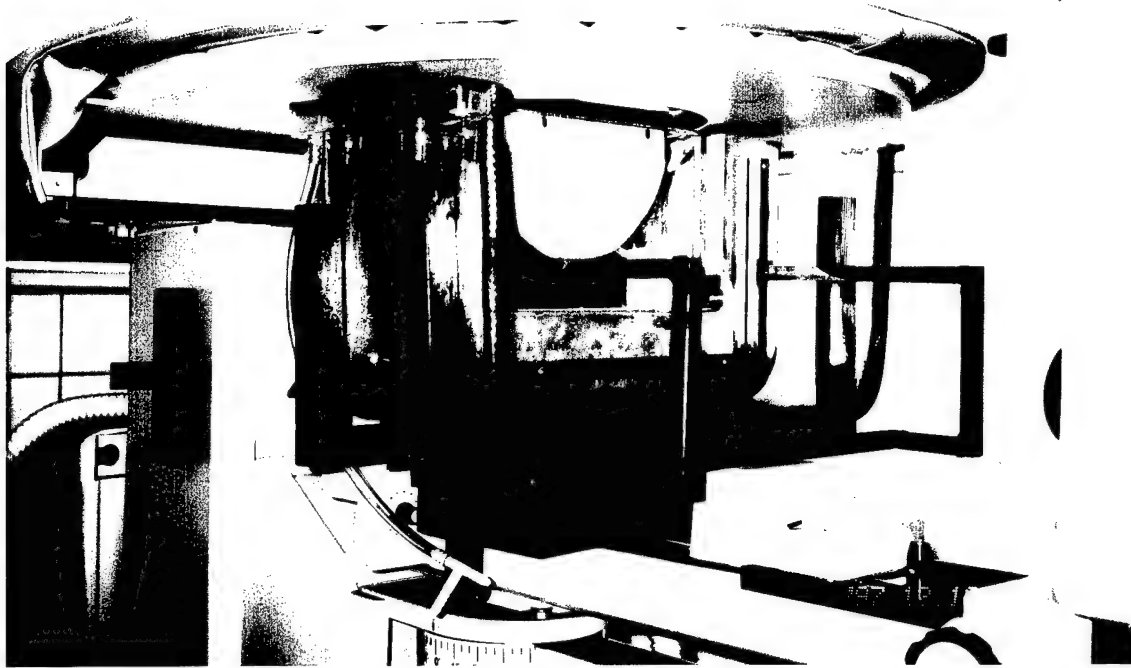


Figure 4(a). Front view of a prototype compressible tank with an x-ray transparent window. During a mammographic procedure, the patient will be in a prone position with the breast to be imaged hanging through the opening on the table and immersed in the tissue-equivalent fluid in the tank.

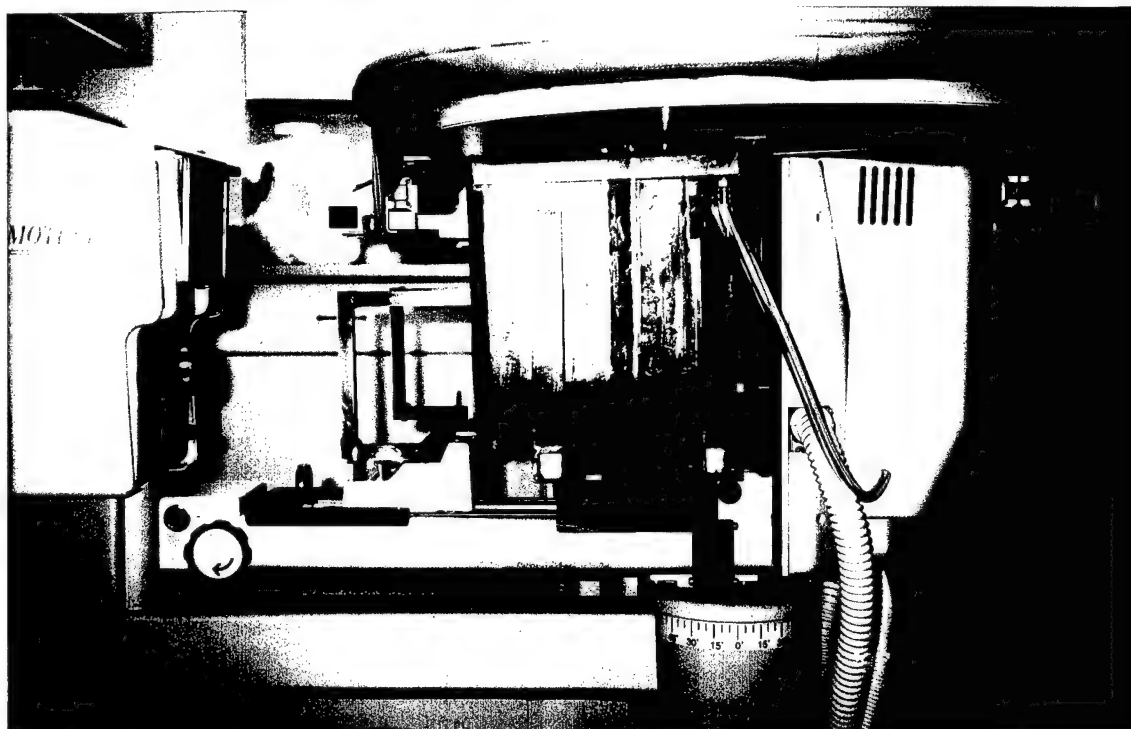


Figure 4(b). Side view of a prototype compressible tank. The compressible tank can be filled with fluid up to the chest wall level and is equipped with a drainage system to prevent overflow of fluid to the x-ray table. The tank can be rotated with the x-ray tube supporting arm to any angle for different mammographic views.

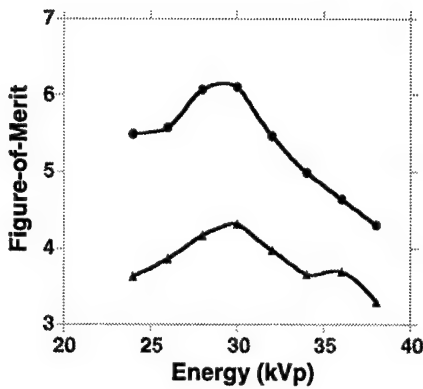


Figure 5. FoM vs. kVp for indirect detectors Gd₂O₂S (top) and CsI (bottom) with a grid.

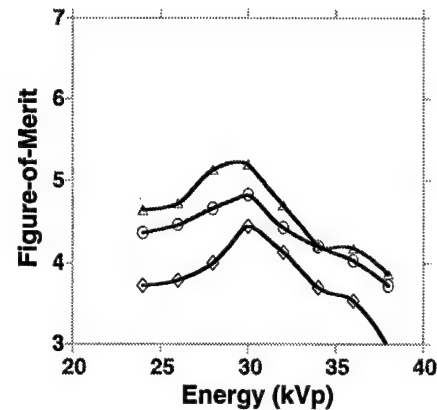


Figure 6. FoM vs. kVp for direct detectors PbI₂ (top), a-Se (middle), and CdZnTe (bottom) with a grid.

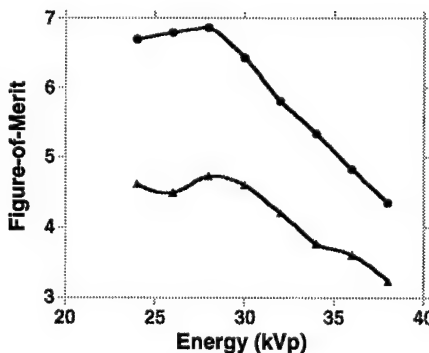


Figure 7. FoM vs. kVp for indirect detectors Gd₂O₂S (top) and CsI (bottom) without a grid.

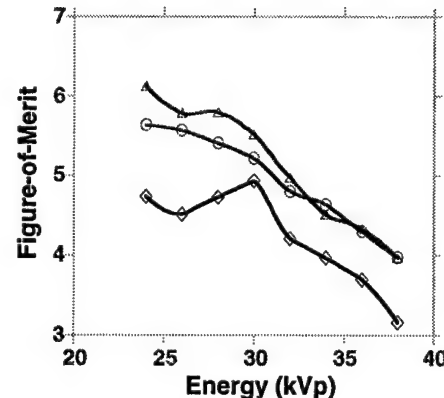


Figure 8. FoM vs. kVp for direct detectors PbI₂ (top), a-Se (middle), and CdZnTe (bottom) without a grid.

(7) Conclusion

During the fourth year of the project, we have (a) completed a simulation study of the effects of equalization and filter misalignment, (b) designed and built a prototype compressible tank for equalization with a prone mammography system, (c) studied the dynamic range and contrast for equalization using the new liquid bolus method, and (d) studied the optimization of mammographic imaging techniques by Monte Carlo modeling. We have demonstrated the feasibility of the original approach of constructing a near-patient specific external filter device for x-ray equalization. We have also investigated the design and construction of a prototype compressible tank for the new approach. We have identified some potential tissue-equivalent liquids that can be used for equalization with the immersion method. The new approach is a

significant step towards the practical implementation of the x-ray equalization technique. The optimal techniques and detectors for mammographic imaging without the dynamic range limitation by the detector are being studied by Monte Carlo modeling. In the no-cost-time-extension year, we plan to continue the investigation of the new equalization technique and the optimization of the mammographic imaging system. Theoretical and experimental investigations will be performed to determine the best liquid bolus material for this application. Realistic phantoms will be designed and built for an experimental test of the method. An improved immersion/compression tank will be developed and built. Finally, additional Monte Carlo simulation studies will be carried out to determine optimum spectra for imaging mammographic lesions within breasts of various sizes and compositions using both detector materials.

(8) References

Baines CJ, Miller AB, Wall C, et al: Sensitivity and specificity of first screen mammography in the Canadian National Breast Screening Study: A preliminary report from five centers. Radiology 160:295-298, 1986.

Baker LH: Breast Cancer Detection Demonstration Project: A Five-Year Summary Report. CA Cancer J Clin 32:194-225, 1982.

Baxter B, Ravindra H, Normann RA: Changes in lesion detectability caused by light adaptation in retinal photo-receptors. Invest Radiol 17:394-401, 1982.

Bick U, Giger ML, Schmidt RA, Nishikawa RM, Doi K. Density correction of peripheral breast tissue on digital mammograms. RadioGraphics 1996; 16:1403-1411

Bunch PC, Huff KE, Van Metter R: Analysis of the detective quantum efficiency of a radiographic screen/film system. J Opt Soc Am A 4:902-909, 1987.

Bunch PC (Personal communication)

Byng JW, Critten JP, Yaffe MJ. Tissue-equalization processing for mammographic images, Radiology 1997;203:564-568.

Chan HP, Doi K, Energy and angular dependence of x-ray absorption and its effect on radiographic response in screen-film systems, Phys Med Biol, 1983;5:565-579.

Constantinou C, Phantom materials for radiation dosimetry. I. Liquids and gels, BJR 1982; 55: 217-224.

D'Agincourt L: Technique is everything when breast is dense. Diagnostic Imaging, September: 57-61, 1993.

Dance DR, Perslid J, Carlsson GA. Calculation of dose and contrast for two mammography grids. Physics Med. Biol. 1992; 37, 235-45.

Fahrig R, Rowlands JA, Yaffe MJ. X-ray imaging and amorphous selenium: Optimal spectra for digital mammography. Med Phys 1996;23:557-567

Hammerstein GR, Miller DW, White DR, Masterson ME, Woodard HQ, Laughlin JS. Absorbed radiation dose in mammography, *Radiology* 1979;130:485-491.

Haug PJ, Tocino IM, Clayton PD, Bain TL: Automated management of screening and diagnostic mammography. *Radiology* 164:747-752, 1987.

Jennings RJ, Fewell TR. Spectral simulation and photon design program suite, FDA, Rockville, MD 20857

Lam KL, Chan H-P. Effects of x-ray beam equalization on mammographic imaging. *Medical Physics* 1990;17: 242-249.

Rezentes PS, de Almeida A, Barnes GT. Mammography grid performance. *Radiology* 1998 (in press).

Sickles EA: Mammographic features of 300 consecutive nonpalpable breast cancers. *AJR* 146:661-663, 1986.

Snyder HL: Chapter 3: The Visual System: Capabilities and Limitations. In: *Flat-Panel Display and CRTs*. Ed. Tannas LE Jr, Van Nostrand Reinhold, New York, 1985.

Storm E and Israel H. Nuclear Data Tables. 1970; A7: 565-81.

Wallis MG, Walsh MT, Lee JR: A review of false negative mammography in a symptomatic population. *Clinical Radiology* 44: 13-15, 1991.

White DR and Constantinou C. Anthropomorphic phantom materials. In *Progress in Medical Radiation Physics, Volume 1*, Orton CC, editor, (Plenum, New York, 1982) pages 133-193.

Wu X, Barnes GT, Tucker DM. Spectral dependence of glandular tissue dose in screen-film mammography. *Radiology* 1991; 179:143-148.

Zhao W and Rowlands JA. Digital radiology using active matrix readout of amorphous selenium: Theoretical analysis of detective quantum efficiency. *Med Phys* 1997;24:1819-1833.

(9) Appendix

Publications in current year as a result of this grant

1. Goodsitt MM, Chan HP, Liu B, Morton AR, Guru SV, Keshavmurthy S, Petrick N. Classification of compressed breast shape for the design of equalization filters in mammography. Medical Physics 25: 937-948, 1998.
2. Keshavmurthy SP, Chan HP, Goodsitt MM. Evaluation of x-ray detectors for digital mammography - Monte Carlo simulation study. Presented at the 83rd Scientific Assembly and Annual Meeting of the Radiological Society of North America, Nov 30-Dec 5, 1997, Chicago, Illinois. Radiology 1997; 205(P): 303.
3. Keshavmurthy SP, Goodsitt MM, Chan HP, Helvie MA. Design and evaluation of an external filter technique for exposure equalization in mammography. Medical Physics (submitted).

Copies of Publications #1 and #3 are enclosed with report.

*Submitted to
Medical Physics*

**Design and Evaluation of an External Filter Technique
For Exposure Equalization in Mammography**

Shyam P. Keshavmurthy, Ph.D.,

Mitchell M. Goodsitt, Ph.D.,

Heang-Ping Chan, Ph.D.

Mark A. Helvie, MD

Department of Radiology
University of Michigan

Corresponding author:

Heang-Ping Chan, Ph.D.

Department of Radiology

University of Michigan

1500 E. Medical Center Drive

Ann Arbor, MI 48109-0030

Office: (734) 936-4357

FAX: (734) 936-7948

e-mail: chanhp@umich.edu

ABSTRACT

We are developing an external filter method for equalizing x-ray exposure in the peripheral region of the breast. This method requires the use of only a limited number of custom-built filters for different breast shapes in a given view. This paper describes the design methodology for these external filters. The filter effectiveness is evaluated through a simulation study on 171 mediolateral and 196 craniocaudal view digitized mammograms and through imaging of a breast phantom. The degree of match between the filter and the individual 3-D exposure profiles at the breast periphery is quantified. A misalignment analysis is performed to investigate the effect of mismatch. The simulation study indicates that the filter is effective in equalizing exposures for more than 80% of the breast images in our database, but artifacts can occur due to large misalignments in the filter position.

Key Words: mammography, equalization, external filtration, and simulation

I. INTRODUCTION

Radiographic contrast plays a crucial role in the detection of subtle lesions that are signs of early breast cancer. Since radiographic contrast decreases with increasing hardness of the x-ray spectrum¹, low energy radiation and high contrast screen/film systems are recommended to maximize the contrast between a lesion and the background breast tissue. The low energy x-rays used in mammography and reduced tissue thickness at the breast periphery result in a large exposure range in a breast image. We have estimated that the exposure range for a 5-cm-thick breast of dense fibroglandular tissue can be as great as 145:1 for a 28 kVp Mo/Mo spectrum. Since a typical high-contrast film used in mammography provides a narrow latitude in the range of about 10:1, it generally cannot accommodate the wide exposure range of a breast image^{2, 3}. The radiographic contrast of mammographic features imaged at the toe and the shoulder regions of the sensitometric curve is greatly reduced. Stacey-Clear et al.⁴ have shown, in their study of breast cancer location in women aged under 50, that 73% of the cancers (63 out of 86) were clearly at the periphery of the breast parenchyma, with the majority near the subcutaneous fat. Since the contrast sensitivity of the human visual system also decreases rapidly with an increase in the film density⁵⁻⁷, the poor image quality in the peripheral region imposes a serious limitation on the sensitivity of cancer detection in breasts with dense fibroglandular tissue. These problems may be reduced if an exposure equalization technique can be developed for mammographic imaging.

Several exposure equalization methods have been proposed to improve mammographic imaging. In one method, a water bag⁸⁻¹⁰ or a solid, elastic, unit density x-ray attenuator¹¹ fills the gap between the breast and the compression paddle to reduce the breast thickness variation in the peripheral region. This method can be patient-specific. However, it may be difficult to implement, especially for oblique views, when using a water bag. Another method involves scanning of the breast with either single or multiple intensity-modulated x-ray beams that are based upon x-ray transmission signals obtained from single or multiple detectors¹²⁻¹⁴. Such a method can equalize the exposure throughout the breast rather than just at the periphery. However, the method is complex, requires much greater heat loading of the x-ray tube than

conventional mammography and much longer exposure times. The latter may result in significant motion artifacts. Better visualization of lesions at the breast periphery can be achieved by display equalization methods such as hot lighting and post-processing of digital images¹⁵. These methods reduce the contrast threshold for perception. However, they do not improve the signal-to-noise ratio of the image.

We have proposed a new exposure equalization method for reducing the dynamic range of the mammograms¹⁶. This method employs a set of external x-ray beam intensity shaping filters that are positioned near the collimator of the mammography system. A similar technique was reported by Boone et al. for equalizing chest radiographs¹⁷. However, no x-ray pre-exposure will be required for filter selection in our approach. The proposed mammography equalization system is shown schematically in Figure 1. A video camera will acquire a color image of a compressed breast. Next, an image segmentation program is employed to extract the breast boundary. This breast border is then classified into a breast shape group. A pre-fabricated exposure equalization filter corresponding to this group will be placed in the beam path and aligned with the breast border by a translation-rotation apparatus operated under computer control. The focal-spot-to-filter distance (D2) can be varied to match different breast sizes. The mirror shown in this figure is used to acquire the TV camera image and will be removed from the beam path before acquisition of the x-ray image.

In an earlier study, Goodsitt et al.¹⁶ demonstrated that compressed breasts can be classified into a finite number of shapes and therefore only a finite number of filters are needed for equalization. In this paper, we report the results of a computer simulation study that was conducted to determine the effectiveness of such a finite number of filters in equalizing the exposures of mammograms.

II. MATERIALS AND METHODS

2.1 Breast boundary detection

1004 clinical mammograms acquired with a dedicated mammographic system with a Mo anode and Mo filter were randomly selected from patient files in our department. All mammograms were recorded with Kodak Min-R/Min-RE screen-film systems. The selected images included both craniocaudal (CC) and mediolateral oblique (MLO) views. The films were

digitized with a DBA Systems, Inc. (Melbourne, Florida) model ImageClear M2100 film digitizer. The light sensor of this system is composed of two linear arrays of charge coupling devices (CCD) that are butted together to form a contiguous array. The system provides a 21-micron pixel size, which is much finer than is required for our application. We operated the digitizer in a mode, in which two of every three pixels were skipped, yielding an effective pixel size of 63 microns. The resolution was further reduced to 1 mm by averaging pixel values in adjacent 16 X 16 pixel regions. The light transmission through the films was digitized in 16-bit linear format. These values were later converted to 12-bit logarithmic format to yield a fairly linear relationship between the film optical density (OD) and pixel value, with larger pixel values corresponding to lower ODs. The pixel value versus OD calibration curve leveled off at an OD of about 3.6, beyond which the pixel values remained almost constant. An automated border-tracking algorithm was applied to the digitized images ¹⁸. Acceptable borders were obtained in 95% of the mammograms (954 of the 1004), and these borders were used to design the external exposure equalization filters.

2.2 Classification of breast shapes

A total of 470 CC-view and 484 MLO-view automatically traced borders were analyzed. In our previous study, we found that the breast borders could be fitted very well with the polynomial $y = ax^2 + bx^3$. This functional form has the advantage of producing only two coefficients (a, b) which can be used in a cluster analysis to classify the border shapes. These coefficients were introduced into a k-means clustering algorithm. Optimal clustering was achieved for three or four groups in both CC and MLO views. The details of this model and its suitability were reported in our earlier study ¹⁶.

2.3 Filter Design

Before building an actual system, we conducted a simulation study to investigate the effectiveness of the external filters. In this simulation study, we designed and implemented an analytical equalization filter for each group of breasts. The a-b polynomial fit discussed earlier describes the projected breast shape on the image, however, it does not account for the thickness variation near the periphery of a

compressed breast. Changes in the breast thickness at the periphery are observed as changes in the gray scale values of pixels on the digitized mammogram. Because equalization occurs in the exposure domain, the pixel values have to be converted to exposure. The conversion involves use of the digitizer calibration curve and the sensitometric curve of the screen-film system. The exposure profiles of the breast periphery estimated from the mammograms can be used to design an average filter for that group.

The calculation procedure used for designing an exposure equalization filter is presented as a flow chart in Figure 2. The average thickness profile of the filter for a given group of classified breasts was estimated from an average exposure profile from all images in the group as follows. For each image, the pixel value profiles along a number of normals (25 to 35) to the automatically detected breast boundary ¹⁸ were obtained. Each normal consisted of 41 points that were 1 pixel apart, of which 20 points were outside the breast and 20 were inside the breast. The 21st point was exactly on the detected breast boundary. Thresholding criteria were employed to exclude pixels where the normals intersected lead markers or the pectoral muscle. The pixel values were converted to optical densities by using the CCD digitizer calibration curve and linear interpolation. The OD profiles along all the normals were averaged to obtain a mean OD profile for each breast. The mean OD profiles for all the breasts in a given group were in turn averaged to obtain an average OD profile for the entire group. This process of multi-step OD averaging ensured that a smooth relative exposure profile was used for filter design. This average OD profile was subsequently converted to a relative exposure profile using a typical sensitometric curve for the Kodak Min-R / Min-RE screen-film system. The conversion from optical density to relative exposure was implemented by semi-log interpolation along the sensitometric curve.

Since our intent was to design filters that correct the primary exposure, the relative exposure profile derived above was corrected for the scatter component. Dance et al ¹⁹ found in an earlier study that the scatter component depends on breast composition and thickness. However, the imaging technique, breast thickness and composition for each of the digitized mammograms used in our study were not known. For the simulation

study, we assumed a scatter fraction of 0.19, which was the scatter fraction that we measured using a beam stop method near the center of an average breast phantom (CIRS, 4.5 cm, 50% gland and 50% adipose) imaged with a grid and a 28kVp Mo/Mo spectrum. The primary exposure was then obtained using the following relationship,

$$\bar{E}_p = \bar{E}_t (1 - SF) \quad (1)$$

where, \bar{E}_p is the mean primary exposure, \bar{E}_t the mean total exposure and SF , the scatter fraction. We ignored the variation of the scatter fraction due to the decreasing thickness in the periphery region of the breast because that variation depends on the thickness profile of a compressed breast and the tissue composition, which were not known from the digitized mammograms.

Ideally, equalization reduces the exposure at the breast periphery to approximately the same as that in the central region of the breast. The average exposure reduction factor at a given point along a normal was therefore derived as the ratio of the minimum relative exposure on the normal to the relative exposure value at that point. A profile of average exposure reduction factors was generated and used to implement an average filter required for equalization of the breasts in a particular group, as follows.

The two-dimensional (2-D) filter shape was obtained by using the mean a and b coefficients of the filter shape polynomial for a given group. The exposure reduction factor profile along each normal to the filter boundary was assumed to be the same as the estimated average exposure reduction factor profile. To obtain a 3-D surface of exposure reduction factors along the breast periphery for the given breast group, the average exposure reduction factor profile was repeated along a set of equally spaced normals to the filter shape polynomial. The exposure reduction factor at any location of the filter was then obtained by 2-D interpolation between two adjacent normals. This matrix of exposure reduction factors that represented the x-ray attenuating function of the filter was used in the simulation study.

To design a physical filter, the average exposure reduction factor profile along a normal was converted to a filter thickness profile using a filter thickness versus exposure reduction factor look-up table as described in the following paragraph. The thickness values at 41 points along a normal were obtained and the thickness profile was swept

along the filter boundary to generate a 2-D matrix of filter thickness using the procedure similar to that described in the previous paragraph. Although the thickness matrix was not used in our simulation study, it is useful for fabricating actual filters.

To generate a filter thickness-to-exposure reduction factor conversion table, a filter material was selected and the attenuation coefficients for this material were obtained using the XCOM²⁰ computer program. The attenuation coefficients were then used in the following relationship to calculate the exposure reduction that could be obtained with a given filter thickness:

$$Es_f(t_f) = \frac{\sum_E f(E) E e^{-\mu_f t_f} \left(\frac{\mu_e(E)}{\rho} \right)_{air}}{\sum_E f(E) E \left(\frac{\mu_e(E)}{\rho} \right)_{air}} \quad (2)$$

where $Es_f(t_f)$ is the filtered relative exposure, also referred to as the exposure reduction factor, $f(E)$ is the relative number of photons at a given energy E of the spectrum, $(\mu_e(E)/\rho)_{air}$ is the mass energy absorption coefficient of air at energy E , $\mu_f(E)$, and t_f are the linear attenuation coefficient at energy E and the thickness of the filter material, respectively. The mass energy absorption coefficients of air were obtained from Johns and Cunningham²¹. This calculation provided a relative exposure of 1 when the filter thickness was zero and a value less than 1 for larger filter thickness. In this study, we assumed a spectrum ($f(E)$) of Mo/Mo 28 kVp with an HVL of 0.32 mm Al²². The exposure reduction factor was stored along with the corresponding filter thickness as a look-up table for use in the filter design procedure.

We can use either solid materials, tissue-equivalent fluids or more radiodense liquids with radiation transparent molds enclosed in a sealed container to build the equalization filters. Figure 3 shows sketches of such liquid and solid filters. Examples of liquids that might be used in filters include water, saline, and water/alcohol solutions. Solid filters might be made of plastic or plastics impregnated with heavy elements.

2.4 Simulation study

To verify the effectiveness of external-filter-based exposure equalization, the entire filtration process was simulated using computer programs and was tested on digitized mammograms. Since the equalization process occurred in the exposure domain, we had to convert the pixel values in the digitized images to relative exposure values. These exposures were filtered and then converted back to pixel values for displaying the filtered image. The various steps in the simulation process are presented as a flow chart in Figure 4.

For a given mammogram to be equalized, the procedure starts by detecting the boundary of the breast image using our automated breast border tracking program. The detected boundary is then fitted with the ax^2+bx^3 polynomial. Using the a and b values, the breast border is classified into a particular group. On the basis of this classification, the average equalization filter designed for that breast group is chosen. The equalization filter is represented by the 2-D array of exposure reduction factors described above. This exposure reduction factor array is rotated and translated along both the X and Y directions to achieve the best alignment between the filter and the breast image. The criterion for best alignment is assumed to be the minimization of the root-mean-square (RMS) distance between the filter boundary and the automatically detected breast boundary. The pixel values from the above breast image are then converted to OD using the digitizer calibration curve. The OD at each pixel is subsequently converted to relative exposure using a typical H&D curve for a Kodak Min-R/Min-RE screen-film system. The relative exposure thus obtained includes both the primary and the scatter components. This total exposure is converted to primary exposure by applying the same mean scatter fraction as that used in the filter design. The mapping functions from pixel value to OD, OD to exposure, and total exposure to primary exposure are similar to the mapping functions used for filter design. The primary exposure is then attenuated by using the exposure reduction factor at a given pixel location. Exposure equalization by the external filter is accomplished at this step. The total exposure is derived from the primary exposure and the scatter fraction using the following relationship:

$$E_t = E_p \left(\frac{1}{1 - SF} \right) \quad (3)$$

The total exposure is subsequently converted back to OD using the H&D curve. This OD is compared with the original OD to obtain the OD decrement for a given pixel. This OD decrement is converted to a pixel value increment using the digitizer calibration curve. Because the conversion in each step involves uncertainties, especially in the shoulder and toe regions of the H&D curve, the 2-D array of pixel value increments contains numerical errors that do not exist in an actual filter. To reduce the fluctuations in the pixel value increments, a 2-D smoothing is therefore performed with a 3X3-pixel kernel on the pixel value increment array before the array is added to the original image.

The forward steps implemented here simulate the filter selection and x-ray filtration processes. The reverse steps convert the equalized image to a screen-film mammogram. Hence, the entire process simulates exposure equalization by an external filter.

Figure 5 shows an example of a mammogram, the corresponding array of exposure reduction factors displayed as a gray scale image, and the array of pixel value increments also displayed as a gray scale image. The dark and gray areas in the background outside the breast indicate that the exposure reduction factor array was rotated and aligned to match the given breast shape. Additionally, the pixel value increment array is approximately a negative image of the exposure reduction factor array.

2.5 Filter misalignment analysis

We designed a Figure-of-Merit (FoM) to evaluate the "goodness of alignment" for our external-filter equalization method. First, approximately 25-35 equally spaced normals to the detected breast border were generated for each breast. The pixel values in the digitized mammograms along these normals were obtained at 31 points. Only 10 points outside the breast boundary were used because we were interested in the artifacts that occurred at the breast periphery. The pixel values along the normals represented the OD profiles at the breast periphery before equalization. The pixel value increments used for equalization of the same image were also obtained along each normal and these values

represented the 3-D profile of the filter. The pixel values decreased from the inside to the outside of the breast periphery; whereas the pixel value increment increased. The complement of the pixel value increment profile was computed by transforming the pixel value increment profile using the following relationship:

$$pixcor(i, j) = \text{Max} [pixinc(j)] + base(i) - pixinc(i, j) \quad (4)$$

where $pixcor(i, j)$ was the transformed pixel value increment, $base(i)$ was the minimum pixel value increment on the i th normal and was obtained by averaging the pixel value increments over the last 10 points inside the breast along the i th normal, $\text{max}[pixinc(j)]$ was the maximum pixel value increment on the i th normal, and $pixinc(i, j)$ is the pixel value increment at the j th point along the i th normal.

The correlation coefficient between the pixel value profile and the transformed pixel value increment profile was defined as

$$corf(i) = \frac{\sum_j (pix(i, j) - mpix(i)) (pixcor(i, j) - mpixcor(i))}{\left[\sum_j (pix(i, j) - mpix(i))^2 \right]^{1/2} \left[\sum_j (pixcor(i, j) - mpixcor(i))^2 \right]^{1/2}} \quad (5)$$

where $pix(i, j)$ and $mpix(i)$ indicate the j th pixel value and the mean pixel value along the i th normal in an unfiltered image. The values $pixcor(i, j)$ and $mpixcor(i)$ are the transformed pixel value increment and the mean transformed pixel value increment, respectively, along the same i th normal. The summation j was over all 31 points along the i th normal. The correlation coefficients for all the normals in a given image were averaged and a mean correlation coefficient was obtained. This mean correlation coefficient was used as the FoM that quantified the match between the filter and the breast image. A good match between the transformed pixel value increment profile and the pixel value profile in the original image would result in an FoM close to 1. A mismatch between the breast periphery and the filter shape in the X-Y plane or a mismatch between the two profiles would result in a lower FoM. The FoM could therefore indicate the goodness of alignment between the breast and the filter in the external exposure equalization method. Furthermore, the FoM could be used to estimate some of the tolerances required for the design of an equalization system.

To study the sensitivity of the FoM to misalignment artifacts in an equalized image, we conducted a misalignment analysis as follows.

From the "optimal" position of alignment, which was determined by minimization of the RMS difference between a breast border and the average filter (described in Section 2.4), we simulated some situations of misalignment by displacing the filter either laterally or transversely. The analytical filter was displaced in either direction by 2, 4 and 6 mm and the corresponding equalized images were generated for some images used in this study. By inspecting the changes in the FoM and the misalignment artifacts on the equalized images at different amounts of filter displacement, we could judge if the FoM could be correlated with the goodness of filter alignment. We also analyzed the histogram of the FoMs for the CC-view and MLO -view group of images at ± 2 mm filter displacements and evaluated the changes in the histograms and the average FoMs. This analysis could provide an estimate of the tolerance for constructing an automated filter alignment device.

2.6 Observer study

The alignment analysis described above provided a mathematical relationship for evaluating the match between the filter profile and the exposure profiles at the breast periphery; however, it did not consider some of the subjective image quality preferences of a human observer.

To test the effectiveness of the filter, 60 images from the CC-view group were randomly selected and were viewed by an experienced radiologist. The quality of the equalized image was ranked between 1 and 5. A quality rating of 1 represented an image with artifacts caused by equalization, and a quality rating of 5 represented an image that exhibited a near perfect equalization. The radiologist also rated the breast density in terms of the ACR-BIRADS ratings.

2.7 Preliminary phantom experiment

To demonstrate the effect of an external filter, we built two types of filters and obtained equalized images of a breast phantom. A 4.5 cm CIRS (CIRS, Inc., Norfolk,

VA) phantom of 50% glandular and 50% adipose composition was chosen to represent an average compressed breast.

The first type of filter was a liquid filter. It consisted of a hand-crafted Styrofoam mold and a container filled with saline ($\approx 3\%$ of NaCl by weight). The size of the Styrofoam mold was calculated by minifying a full scale drawing of the CIRS phantom. A geometric minification factor of 3 was assumed for this calculation. Two paper templates with different minification factors were made to represent the top and the bottom surfaces of the filter mold. These two pieces were pasted on to an approximately 2-cm-thick Styrofoam sheet and the filter mold was then carved out using the paper templates as a guide. When the container was filled, the thickness of water was 2 cm outside the mold and it gradually decreased to less than 1 mm over the top of the mold. Care was taken to make sure that the liquid layer over the mold covered the entire field of view. This design ensured that there was minimal beam hardening over the central region of the breast and there were no artifacts due to a discontinuity of the liquid filter material at the breast boundary.

The second type of filter was a solid filter. It consisted of a piece of Teflon attached to a thin Plexiglas plate. The Plexiglas plate was used to protect the thin edge of the Teflon filter. The solid Teflon piece was machined using a computer controlled mill to a wedge shape that approximated an equalization filter. The Teflon filter is a 5-cm-wide rectangular strip that has a maximum thickness of 1.8 cm. As a prototype, it was not fabricated to match a breast shape in the X-Y plane.

For each filter, the filter-to-phantom distance and the filter orientation were adjusted manually to obtain the best alignment between the filter and the breast phantom to acquire exposure equalized images.

III RESULTS

3.1 Simulation study

The breasts in the CC or the MLO views were classified into three groups ¹⁶. To have reasonable statistics, we chose the largest group in each view as case samples for our simulation study. The CC-view group contained 196 images and the MLO-view group

contained 171 images. For each of these groups, we could estimate the mean exposure range as the ratio of the maximum to the minimum exposures along the average relative exposure profile (described in Section 2.3). These exposure ranges were found to be 5.46:1 and 5.18:1 for CC and MLO views, respectively. These exposure ranges are lower than what we would expect from breast images and will be discussed further in the Discussion section. Using the average exposure reduction factor array and the steps described in Section 2.3, the pixel value increment array and the equalized image were computed for each mammogram in the group. Figures 6 presents examples of the unequalized and equalized images from the CC and the MLO groups. Figures 7 shows additional examples of equalized images from the CC and MLO view groups.

3.2 Observer study

A histogram of the equalization quality rating by the radiologist is shown in Figure 8. It can be seen that about 81 % of the images had ratings greater than or equal to 3. The radiologist rated 6 images to have a breast density of 1, 31 to have a density of 2, and 16 to have a density of 3, and 7 to have a density of 4.

3.3 Preliminary phantom experiment

The images of the CIRS phantom before and after equalization with saline as a filter material are shown in Figure 9. It can be seen that the filter equalized the periphery region around the nipple reasonably well. However, it under-compensated the periphery in the upper and lower parts of the image. This was probably caused by the mismatch between the filter boundary and the breast border in these regions because the shape of the handcrafted mold did not match very well with the breast phantom shape in the X-Y plane. The 0.4-cm-thick fatty skin layer in the CIRS phantom is clearly visible in the equalized image near the nipple region. Some dark spots seen in this image were due to air bubbles entrapped near the mold.

Images of the CIRS phantom before and after equalization with a Teflon filter are shown in Figure 10. A piece of silly putty was added on the phantom to simulate dense parenchyma in a breast. The filter strip is oriented approximately in the 4 o'clock

direction in the equalized image. The fatty skin layer in the CIRS phantom and some calcium carbonate specks placed near the periphery are clearly visible in the region equalized by Teflon filter. The contrast of the edge of the simulated dense parenchymal region also increases in the equalized image. This is expected to improve detectability of abnormalities in the periphery of the parenchyma.

3.4 Misalignment analysis

The histograms of the FoM for the CC- and MLO-view images at the optimal filter position are plotted in Figure 11.

Equalized images with 0 mm and ± 6 mm displacements of the filter in the lateral and the transverse directions are shown in Figure 12. The FoMs that were calculated for each image are also shown.

The distribution of the FoMs at ± 2 mm filter displacement was also analyzed. The mean FoM and the percentages of images that had FoM values less than or equal to 0.8 were tabulated in Table 1.

IV. DISCUSSION

4.1 Effectiveness of external exposure equalization method

It can be seen in Figure 6 that the equalization along the breast peripheries is very good in these examples, despite the fact that the filter was designed by using an average exposure profile for a given breast shape class. It can also be seen from Figure 7 that although the sizes and shapes of the breasts varied over a wide range, the average filter was effective in equalizing these images without obvious artifacts. Digitizer artifacts due to the unbalanced sensitivity of the two CCD arrays, charge transfer, and blooming can be seen on some of the images. The digitizer artifacts are specific to this simulation study and will not exist in an actual equalization process. These examples illustrate that a small number of external filters can be designed to provide effective equalization at the breast periphery for breasts in a given mammographic view.

4.2 Observer study

Although the data set used in this observer study was small, the radiologist's quality ratings (Fig. 8) demonstrate that the image quality for most of the equalized images was greater than or equal to 3 which can be considered acceptable. The average quality rating was 3.3 for images with breast density ratings of 1 and 2, and it was 4.1 for images with breast density ratings of 3 and 4. The lower average quality rating for the images with lower breast density is probably caused by the fact that they are more likely to be over-compensated by the average filter. This is consistent with the radiologist's suggestions after reviewing the images in the observer study that: (1) slight under-compensation and images with dark rim are in general preferred, (2) any over-compensation and equalized breast images with a low-OD boundary are undesirable, and (3) small fatty breasts do not require equalization.

4.3 Misalignment analysis

For the example shown in Figure 12, the RMS difference between the breast border and the filter border at the "optimal" alignment position (0,0) was 2.13 mm and the FoM was 0.89. There is a dark boundary around the upper section of the breast border due to the slight misalignment as indicated by the RMS error. Displacing the filter by 2 mm in the negative lateral direction reduced the dark rim in the upper border section to lower OD and the FoM increased to 0.90. As the filter was displaced transversely away from breast, the FoM reduced to 0.87, 0.82 and 0.77 for 2, 4 and 6 mm displacements, respectively. The OD along the breast periphery increased as the displacement increased, indicating increasing under-compensation by the filter. On the other hand, when the filter was displaced in the negative transverse direction, the breast periphery became increasingly over-compensated and the FoM reduced to 0.86, 0.84 and 0.79 for 2, 4, and 6 mm displacements, respectively. Except for the -2 mm displacement discussed above, a similar reduction in FoM was also observed for filter displacements along the lateral direction. This example illustrates the effectiveness of the correlation coefficient in quantifying the degree of misalignment. Such a misalignment study was conducted on several MLO and CC view breast images and it was found that the decrease in the FoM was slightly greater for under-compensation artifacts than for over-compensation

artifacts. Additionally, images with an FoM greater than 0.8 did not have significant artifacts in the breast periphery.

It can be seen in Figure 11 that the mean FoM for the group of CC-view images is 0.89 and over 93% of the images had an FoM greater than 0.8. Only 12 of the 196 images had an FoM less than or equal to 0.8 and the minimum FoM is 0.72. Similarly, for the group of MLO view images the mean value of FoM in the histogram is 0.85 and about 81% of the images had an FoM greater than 0.8. Again only 33 of the 171 images have an FoM less than or equal to 0.8. Thus, the average filter shape matched well with over 80% of the images in a given group.

The results in Table 1 indicate that a 2-mm displacement did not reduce the FoM substantially for the CC-view images. The fraction of images with FoM greater than 0.8 was over 88% for displacements in all directions. For the MLO-view images, the mean FoMs for displacement in all directions were still greater than 0.8. However, the fraction of images with an FoM greater than 0.8 decreased to a minimum of 71%. Because the shapes of MLO images are more complicated than CC-view images, the simple polynomial used for the filter shape probably cannot tolerate misalignment as well as in a CC-view. This may have to be improved through shaping of the filter thickness profile so that less equalization is performed at the pectoral and lower breast regions, or through a more complicated filter shape. The latter approach may increase the number of filters required for the MLO view.

From the filter displacement simulation, we estimated that a misalignment of up to 2 mm between the filter edge and breast boundary is tolerable for the CC-view. However, for the MLO-view, the misalignment may have to be less than 1 mm. Because the simulation study used digitized mammograms and an analytical filter, the misalignment occurred in the image plane. However, in actual implementation the filter will be about 20 cm from the focal spot. With such a geometry, the 1 mm corresponds to about 0.3 mm in the filter plane. Such a tolerance is achievable through commercially available X-Y translators. Thus, we expect that it is feasible to build an automatic filter selection and alignment system economically.

4.4 Technical difficulties associated with using digitized mammograms for estimating relative exposure

As discussed earlier, the digitizer calibration curve was used to convert pixel values to OD. These OD values were subsequently converted to relative exposure values by using the screen-film H&D curve. The images used in this simulation study were digitized over a six-month period and during this time the digitizer calibration might have fluctuated. To study this fluctuation, the digitized images were sorted chronologically and the background pixel values in these images at a distance of approximately 1 cm from the breast boundary were analyzed. It was found that sets of consecutive images could be partitioned into four background pixel value ranges. This range was between 980 and 1380. A few images with background pixel values less than 980 were eliminated from the database to limit the range of fluctuation in the digitizer calibration. Since we were not aware of the digitizer fluctuation during the acquisition of the images, we did not have the exact calibration of OD to pixel value for each image. To compensate for this variation, four representative calibration curves were derived by shifting the measured digitizer calibration curve along the pixel value axis by equal increments of 100 while keeping the shape of the calibration curve the same. The calibration curve employed in the equalization process was selected based on the background pixel value in a digitized mammogram. Although this is not an accurate method to address the drift problem in the digitizer calibration curve, it is a simplified approach that provided a reasonable conversion from pixel value to optical density, and the simulation study did serve the purpose of demonstrating the feasibility of our external filter equalization approach.

The 1004 mammograms that were digitized for the breast shape analysis study were acquired between 1992 to 1995 with the majority of images acquired in 1994 and 1995. Because the specific H&D curve for a particular image was not known, we employed a typical H &D curve for Kodak Min-R/Min-RE screen-film system²³ for estimating the relative exposure from the OD. Since the properties of the Kodak Min-R /Min-RE screen-film system were significantly different prior to 1993, all images acquired prior to 1993 were excluded. A typical H &D curve for the Min-R/ Min-RE system in 1994 was used for the sensitometric conversion of all images used in the

simulation study. Additionally, some images with grid lines, breast implants or severe digitizer artifacts were also eliminated.

Because of the technical limitations described above, the database was reduced to 415 CC-view and 411 MLO-view images. The largest CC- and MLO-view groups obtained from cluster analysis contained 196 and 171 images, respectively. These two groups were used in our simulation study.

In addition to the above approximations, we also noticed that the CCD digitizer created artifacts in the digitized images. The main artifact was due to sensitivity mismatch between the two linear CCD arrays. This artifact was seen as a step change in the pixel values at the interface between the two CCDs. Some charge transfer and blooming artifacts (saturation trails) of CCDs were also seen around locations with low ODs. On examination of the images in our data set, we found that the step change artifact occurred at about half the width of an image and that the first strip was brighter than the second. To avoid this step discontinuity, only the normals that did not cross the center line of the images were used for the exposure profile estimation and the FoM calculations. Additionally, pixel value thresholding was used to avoid regions with low OD artifacts while calculating the relative exposure values.

The average exposure range values presented earlier were lower than an expected range of 20:1 for a typical mammogram. To understand this discrepancy, histograms of maximum exposure ranges in each image for the CC- and MLO-view image groups were generated. The maximum exposure range in an image was estimated as the ratio of the maximum to the minimum exposures among all exposure profiles along a set of normals in that image. The histograms of the maximum exposure ranges are shown in Figure 13. The mean values for the CC- and MLO-view histograms are 10.24 and 9.97, respectively, which are still lower than the expected dynamic ranges of breast images. A major reason for underestimation of the exposure range in the digitized mammogram is the inability of the digitizer to digitize accurately in the high OD region. The OD-to-pixel value calibration curve of the digitizer leveled off at about 3.6 OD whereas the maximum OD of mammography film can be greater than 4. Any OD above 3.6 essentially was digitized to about the same pixel value. The OD converted from a pixel value in the breast

periphery therefore could be greatly underestimated. This problem was further amplified by the small gradient in the shoulder region of the H&D curve; a small error in OD corresponded to a large error in relative exposure. Another reason for the small exposure range from our estimation is that searching for the minimum exposure along the selected normals did not guarantee that the densest region in the breast image would be found. The extreme dynamic range of breast images is usually estimated from the densest region (OD near fog and base level) relative to the maximum exposure outside the breast region.

Despite the technical problems described above, our simulation study allowed us to evaluate the feasibility of x-ray equalization with the external filter method, and to examine potential misalignment artifacts.

4.5 Drawbacks of external exposure equalization method

The equalization filter may cause artifacts on some images. These artifacts are mainly due to mismatches between the equalization filter and the breast.

A part or the entire edges may appear brighter than the surroundings. This is an artifact of over-compensation, which arises when a part or the entire filter extends too far into the breast and/or the slope of the filter is greater than that needed to compensate for the exposure gradient at the periphery of the breast. Over-compensation may result in contrast reduction because of the low gradient in the toe region of the H&D curve.

A dark rim or dark areas may appear around the breast. This is an artifact caused by under-compensation. It arises when a part or the entire filter is positioned too far outside the breast or when the slope of the filter is less than that needed to compensate for the exposure gradient at the periphery of a particular breast. Under-compensation is likely to be more acceptable to radiologists because the breast periphery is improved even if it is not completely equalized. This is confirmed by the impression of the radiologist who evaluated the equalized images in the observer study.

Figure 14 shows examples of images from the CC and MLO groups that demonstrate some of these artifacts. These images show regions of over-compensation artifact along the lower portion of the breast border.

One problem revealed by the simulation study of the equalization system is that a single filter thickness for all breasts in one group may not be adequate. It is known that breast density and thickness do change the required amount of exposure compensation for equalization. The rightmost image in Figure 7(a) shows that the image background is brighter than the breast, indicating that the filter was thicker than that needed for this breast. The rightmost image in Figure 7(b) shows an under-compensated image with a background darker than the breast, which indicates that the filter was thinner than that needed for this breast. In actual implementation, the mismatch due to breast thickness can be reduced by building three filters with different thicknesses for each breast shape group; one of these filters may be selected depending on the breast thickness. A criterion can also be set so that no equalization will be used for breasts thinner than a threshold thickness. Although the number of filters will increase by three fold, the total number of filters is still reasonably small and may be acceptable.

For this simulation study, we used a single exposure profile to generate the filter profile along the entire breast border. It can be seen from Figure 7(b) that, in equalized MLO-view images, the pectoral muscle regions are generally over-compensated relative to the breast region. This result indicates that a uniform filter profile along the entire breast border is not a good approximation for the MLO-view images. A solution to this problem may be making the filter thickness gradually taper off in the pectoral muscle region for the MLO groups.

4.6 Implementation of a exposure equalization system

The simulation study used a digitized mammogram as the input image. However, in actual implementation a digital video image of the compressed breast will be used for selection and alignment of the filter. A color video image of the compressed breast can be acquired with dark green background to facilitate segmentation and breast shape classification. Experiments in our laboratory have shown that compressed body parts have a higher red component. A red component image of the compressed breast can be segmented easily from a dark green background by simple thresholding. The breast shape as determined from the segmented boundary may need corrections for potential

differences in the geometry of the video and x-ray images. The algorithms developed here for the simulation study can then be used for breast shape classification, filter selection, and alignment of the filter with the breast boundary.

IV. CONCLUSIONS

We have demonstrated the effectiveness of an exposure equalization technique for mammographic imaging using a small set of near patient-specific external filters. Through a computer simulation study on a large set of digitized CC-and MLO-view breast images, it is shown that an average filter for a group of breasts with a similar shape can be designed using a polynomial to represent the breast shape and an average exposure profile to derive the thickness distribution. This average filter is effective in providing exposure equalization without significant misalignment artifacts for approximately 80% of the images used in this study. Additionally, it is shown that slight misalignment of the filter is tolerable.

A preliminary phantom study using handcrafted filters indicates that it is feasible to fabricate an external exposure equalization filter using either a solid filter material or a negative mold with a liquid filter material.

ACKNOWLEDGMENTS

This work was supported by a grant DAMD 17-94-J-4292 from the U. S. Army Medical Research and Materiel Command. The content of this publication does not necessarily reflect the position of the government and no official endorsement of any equipment and product of any companies mentioned in the publication should be inferred.

Table 1. The effect of 2-mm filter displacement on the FoM for the CC-view and MLO-view images.

Filter Displacement	CC-view group		MLO-view group	
	Mean FoM	% Images $FoM \leq 0.8$	Mean FoM	% Images $FoM \leq 0.8$
0 mm *	0.89	6%	0.85	19%
Transverse +2 mm	0.87	12%	0.83	29%
Transverse -2 mm	0.90	8%	0.86	16%
Lateral +2 mm	0.88	12%	0.84	24%
Lateral -2 mm	0.90	5%	0.85	16%

* Filter location determined by minimum RMS criterion.

V. REFERENCES

1. Gingold EL, Wu X, Barnes GT, "Contrast and Dose with Mo-Mo, Mo-Rh, and Rh-Rh target-Filter combinations in mammography," *Radiology* 195, 639-644 (1995).
2. Maidment A, Fahrig R, Yaffe MJ, "Dynamic range requirements in digital mammography," *Med. Phys.* 20, 1621-1633 (1993).
3. Bunch PC, Huff KE, Van Metter R, "Analysis of detective-quantum efficiency of radiographic screen/film system," *J. Optical Society of America-A* 4, 902-909 (1987).
4. Stacey-Clear A, McCarthy K A, Hall D A, Spellman E P, White G, Hulka C A, Whitman G J, Halpern E F, Kopans D B, "Mammographically detected breast cancer in women under 50 years old," *Radiology* 186, 677-680 (1993).
5. Blackwell HR, "Contrast thresholds of the human eye," *J. Optical Society of America*, 36, 624-643 (1946).
6. Baxter B, Ravindra H, Normann RA, "Changes in lesion detectability caused by light adaptation in retinal photo-receptors," *Inv. Radiol.*, 17, 394-401 (1982).
7. Snyder HL, "Chapter 3: The Visual System: Capabilities and limitations," In: *Flat-Panel display and CRTs*. Ed. Tannas LE Jr. (Van Nostrand Reinhold, New York, 1985).
8. Lam KL, Chan HP, "Development of x-ray beam equalization technique in mammography," *Radiology* 169 (P), 338 (1988).
9. Lam KL, Chan HP, "Exposure equalization technique in Mammography," *Investigative Radiology* 24, 154-156 (1989).
10. Lam KL, Chan HP, "Effects of x-ray beam equalization on mammography imaging," *Med. Phys.* 17, 242-249 (1990).
11. Panayiotakis G, Likaki H, Kolitsi Z, Dimopoulos J, "An anatomical filter for exposure equalization in mammography," *Radiology* 15, 15-17 (1992).
12. Sabol JM, Soutar IC, and Plewes DB, "Mammographic scanning equalization radiography," *Med. Phys* 20, 1505-1515 (1993).
13. Oestmann JW, Stoel B, Schrijvershof H, Vrooman J, and Schultze Kool LJ, "Scanning equalization mammography: Preliminary evaluation," *Radiographics* 14, 123-128 (1994)

14. Sabol JM, Soutar IC, and Plewes DB, "Practical application of a scan-rotate equalization geometry to mammography," *Med. Phys.* 23, 1987-1996 (1996).
15. Byng JW, Critten JP, Yaffe MJ, "Thickness-equalization processing for mammography images," *Radiology* 203, 564-568 (1997).
16. Goodsitt MM, Chan HP, Liu B, Morton AR, Guru SV, Keshavmurthy S, Petrick N, "Classification of compressed breast shape for the design of equalization filters in mammography," *Med. Phys.* 25, 937-948 (1998).
17. Boone JM, Duryea J, Steiner RM, "Filter wheel equalization for chest radiography: A computer simulation," *Med. Phys.* 22, 1029-1037(1995).
18. Morton AR, Chan HP, Goodsitt MM, "Automated model-guided breast segmentation algorithm," *Med. Phys.* 23, 1107-1108 (1996).
19. Dance DR, Perslid J, Carlsson GA, "Calculation of dose and contrast for two mammography grids," *Phys. Med. Biol.* 37, 235-245 (1992).
20. Berger MJ, Hubbell JH, XCOM: Photon cross sections on a personal computer, US Department of commerce, National bureau of standards, Gaithersburg, MD, NBSIR 87-3597 (1987).
21. Johns HE and Cunningham JR, *The Physics of Radiology* 4th Ed. (Charles C. Thomas, Springfield, IL, 1983).
22. Jennings R.J, "Spectral simulation and photon design program suite," FDA, Rockville, MD 20857 (1993).
23. Moore W.E, "Estimated sensitometric data for Kodak Min-R E film," Personal Communication, Eastman Kodak Company, Rochester, NY (1995).

LIST OF FIGURES

Figure 1. Schematic of a mammography unit implemented with an equalization filter system

Figure 2. Procedure for designing an external equalization filter.

Figure 3. Schematics of fabricating filters with (a) liquid or (b) solid material

Figure 4. Flow diagram of the simulation study for evaluation of the effects of x-ray equalization on mammograms.

Figure 5. An example of (a) a digitized mammogram (b) an exposure reduction factor matrix displayed as a gray scale image, and (c) the corresponding pixel value increment matrix.

Figure 6. Examples of (a) unequalized and equalized CC-view images, (b) unequalized and equalized MLO-view images

Figure 7. A set of (a) CC-view and (b) MLO-view images obtained using external exposure equalization technique. These images used an average filter specific to their group and all the CC-view images are from the same group, similarly, all the MLO-view images belonged to a single group.

Figure 8. Distribution of equalization quality ratings for 60 equalized images, evaluated by an experienced breast radiologist.

Figure 9. CIRS phantom image (a) unequalized and (b) equalized with a liquid filter.

Figure 10. CIRS phantom image (a) unequalized and (b) equalized with a solid filter made with Teflon. A piece of silly putty was placed on top of the phantom to simulate dense breast parenchyma and calcium carbonate specks were placed at the periphery. The visibility of the peripheral region of the dense parenchyma and of the breast phantom is improved by equalization.

Figure 11. Distribution of the Figure-of-Merit for the group of (a) CC-view and (b) MLO view images.

Figure 12. Effect of filter misalignment on the FoM. The dark areas seen along the breast periphery are due to under-compensation whereas the lighter areas are due to over-compensation. The numbers in parentheses indicate the filter displacements and the numbers at the upper left corner are the corresponding FoM values.

Figure 13. Histogram of maximum exposure range for the group of (a) CC-view and (b) MLO-view images.

Figure 14. Example of images with artifacts: (a) unequalized CC-view image (left) and equalized image with under-compensation artifact (right) in the upper portion and below the nipple, (b) unequalized MLO-view image (left) and equalized image with over-compensation artifact (right) in the lower portion of the breast periphery.

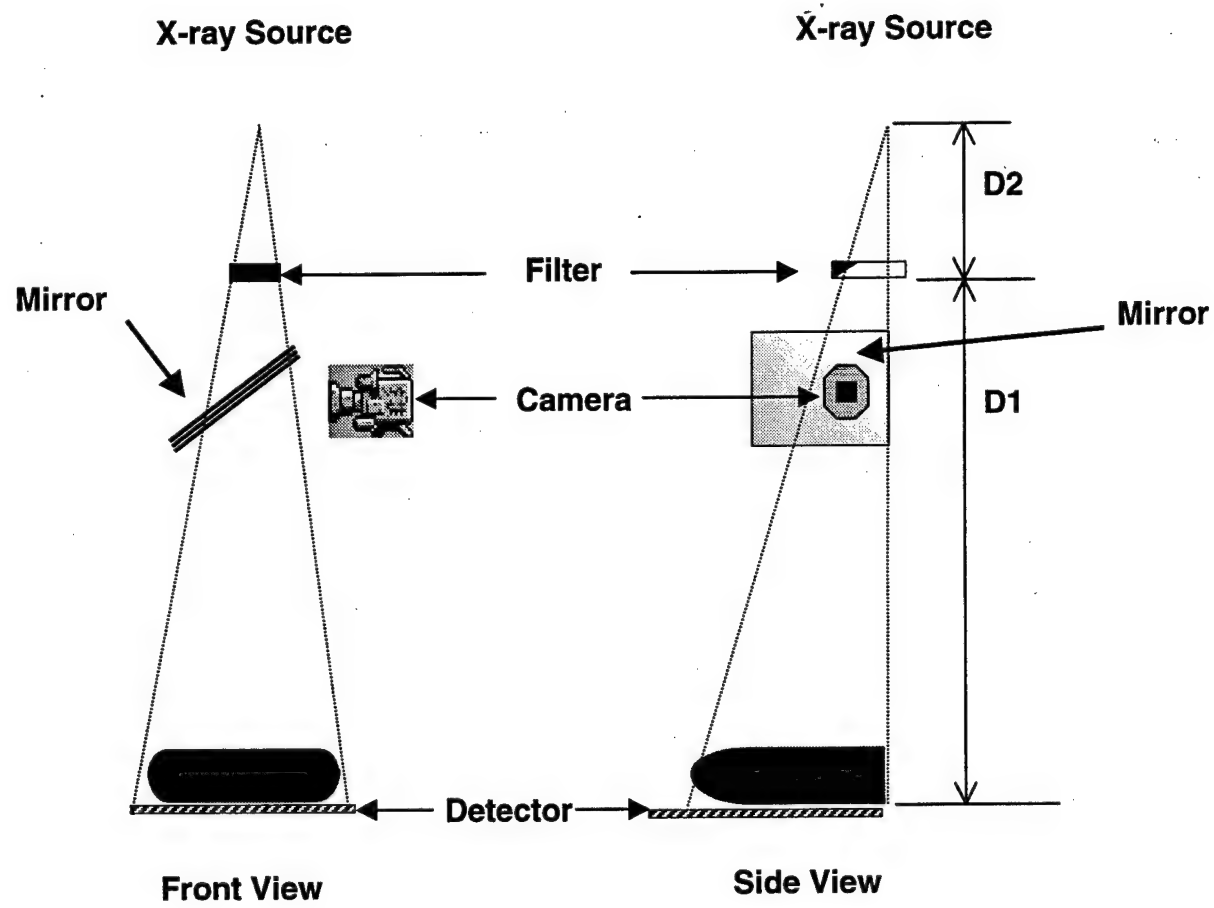


Figure 1. Schematic of a mammography unit implemented with an equalization filter system

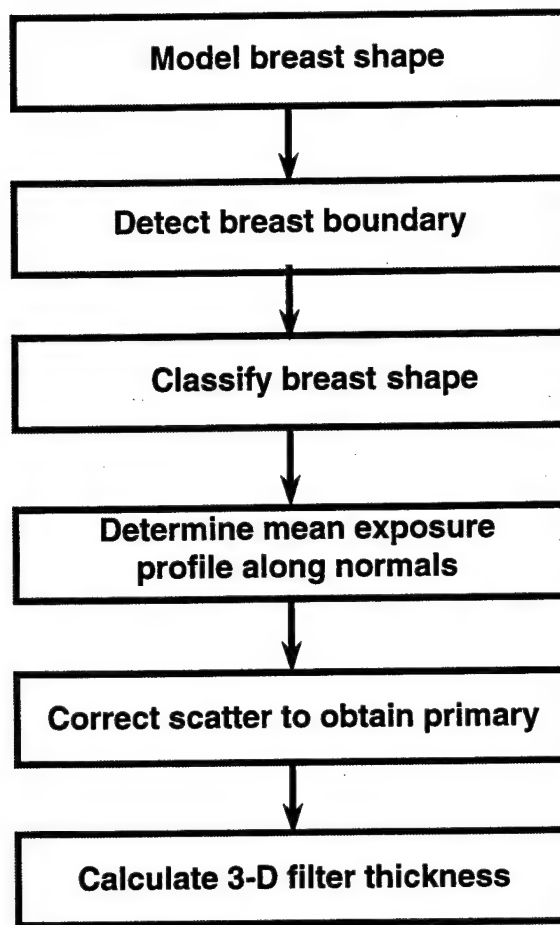
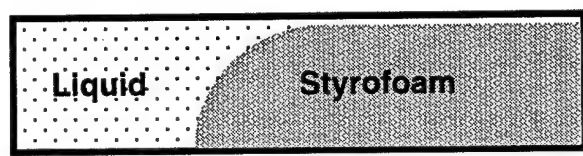
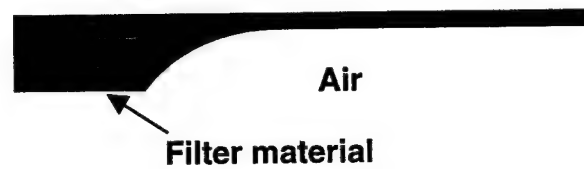


Figure 2. Procedure for designing an external equalization filter.



(a)



(b)

Figure 3. Schematics of fabricating filters with (a) liquid or (b) solid material

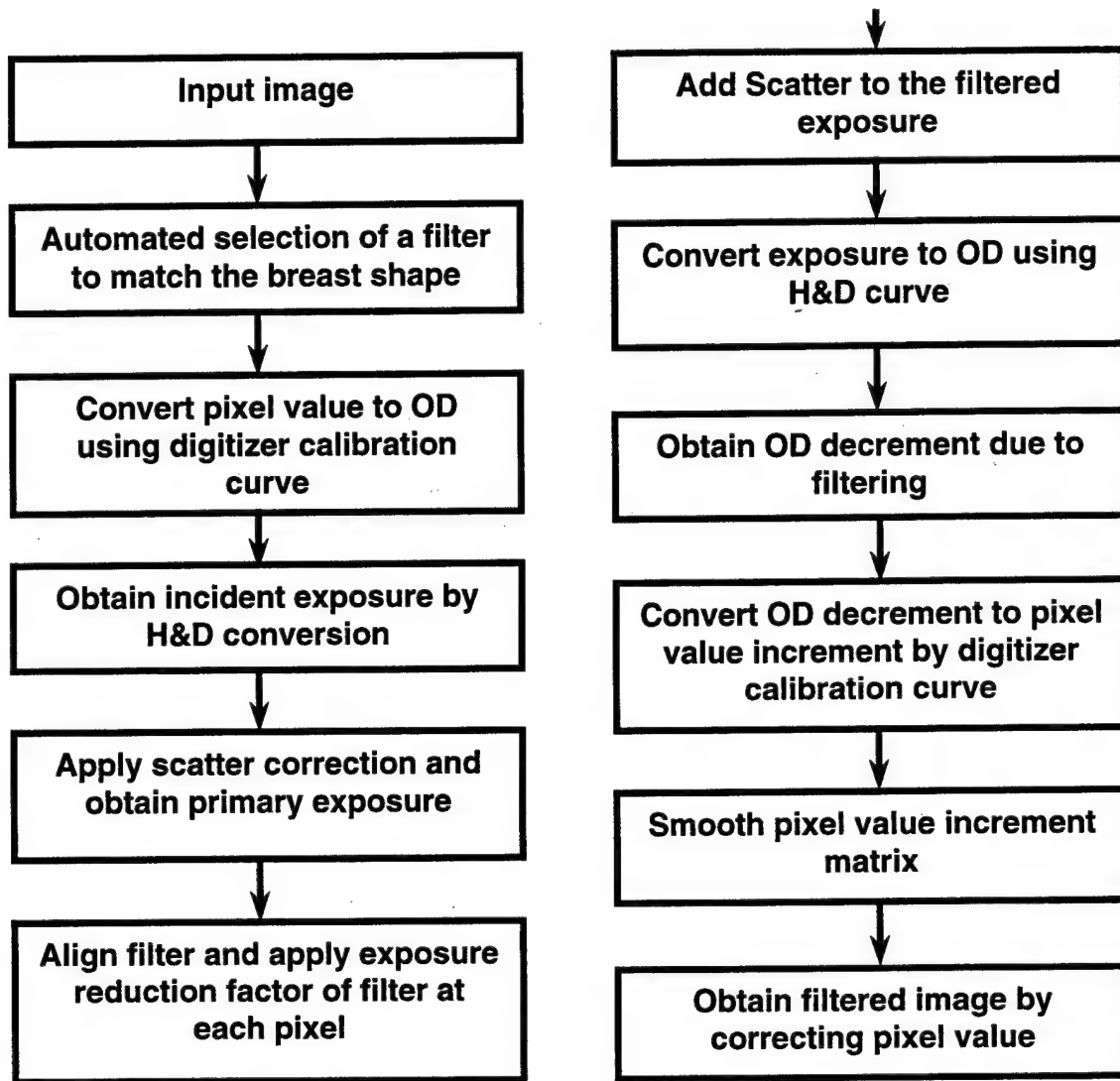


Figure 4. Flow diagram of the simulation study for evaluation of the effects of x-ray equalization on mammograms.

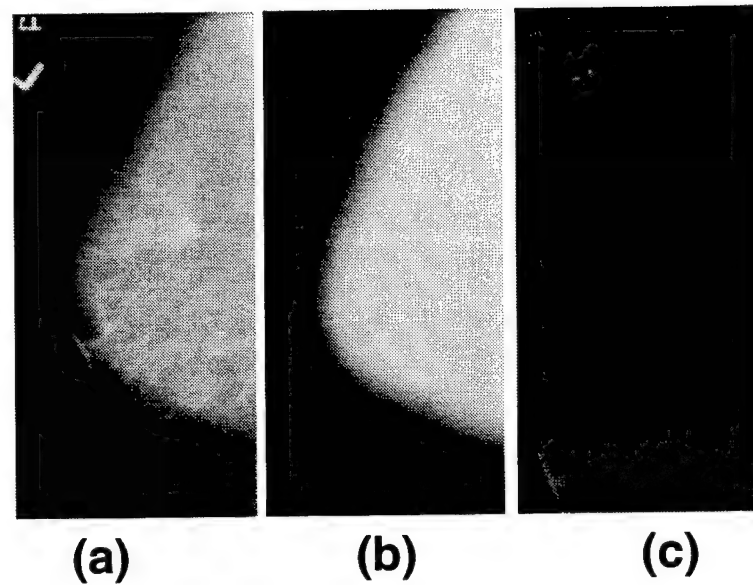
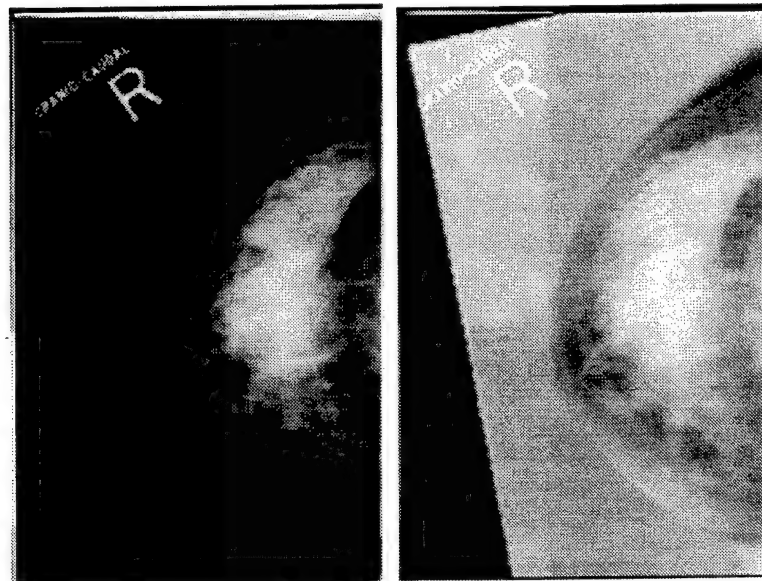
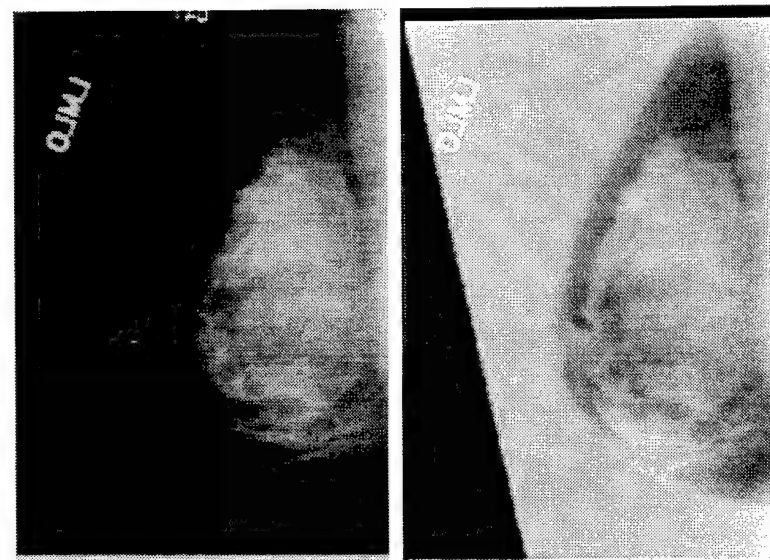


Figure 5. An example of (a) a digitized mammogram (b) an exposure reduction factor matrix displayed as a gray scale image, and (c) the corresponding pixel value increment matrix.

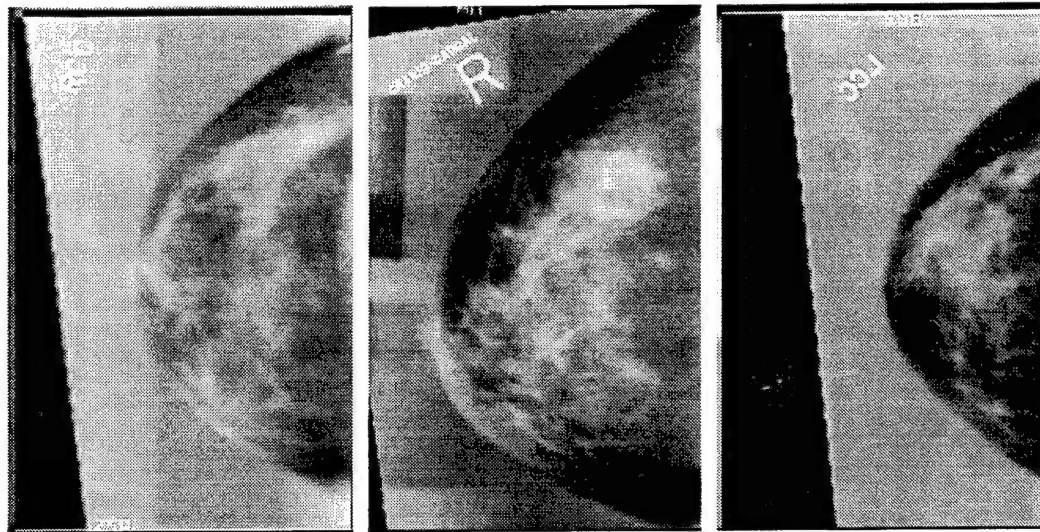


(a)

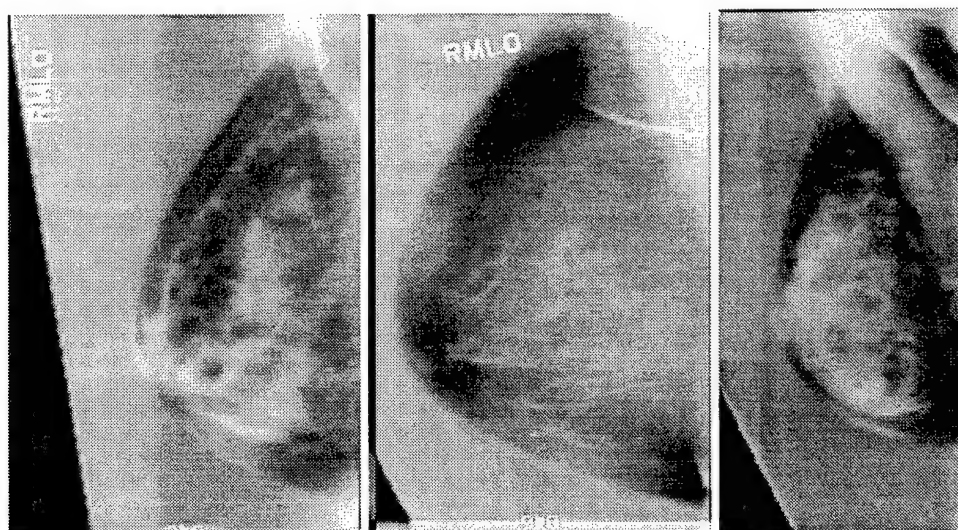


(b)

Figure 6. Examples of (a) unequalized and equalized CC-view images, (b) unequalized and equalized MLO-view images.



(a)



(b)

Figure 7. A set of (a) CC-view and (b) MLO-view images obtained using external exposure equalization technique. These images used an average filter specific to their group and all the CC-view images are from the same group, similarly, all the MLO-view images belonged to a single group.

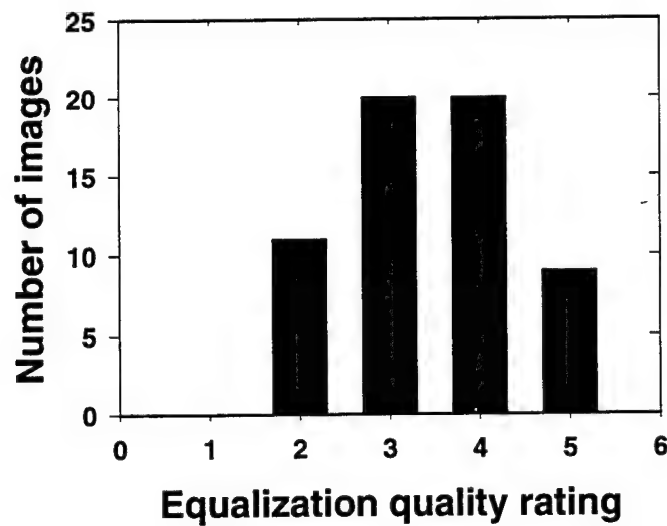
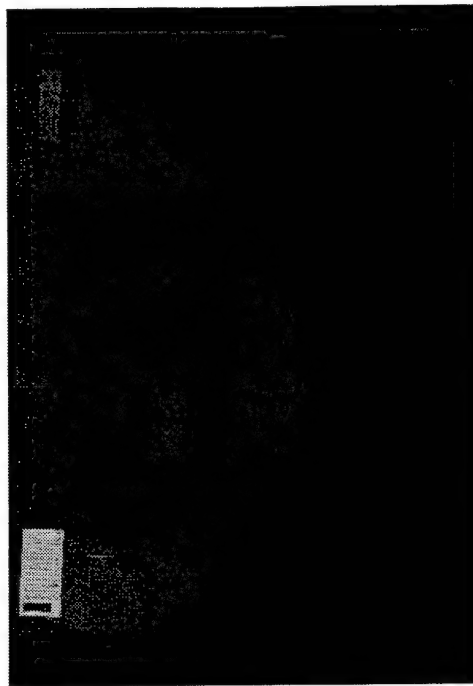
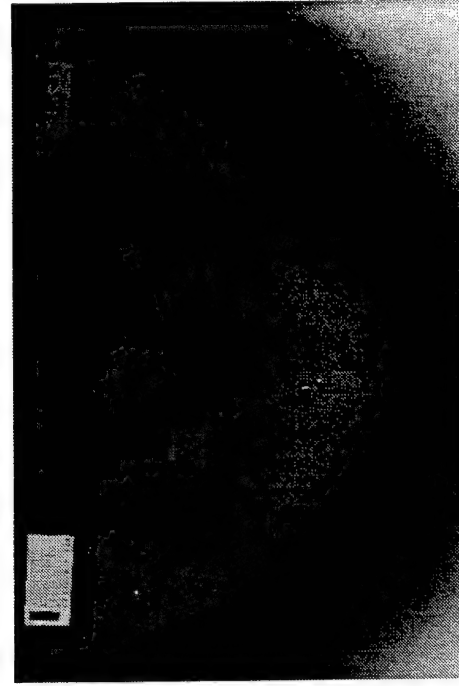


Figure 8. Distribution of equalization quality ratings for 60 equalized images, evaluated by an experienced breast radiologist.



(a)



(b)

Figure 9. CIRS phantom image (a) unequalsized and (b) equalized with a liquid filter.

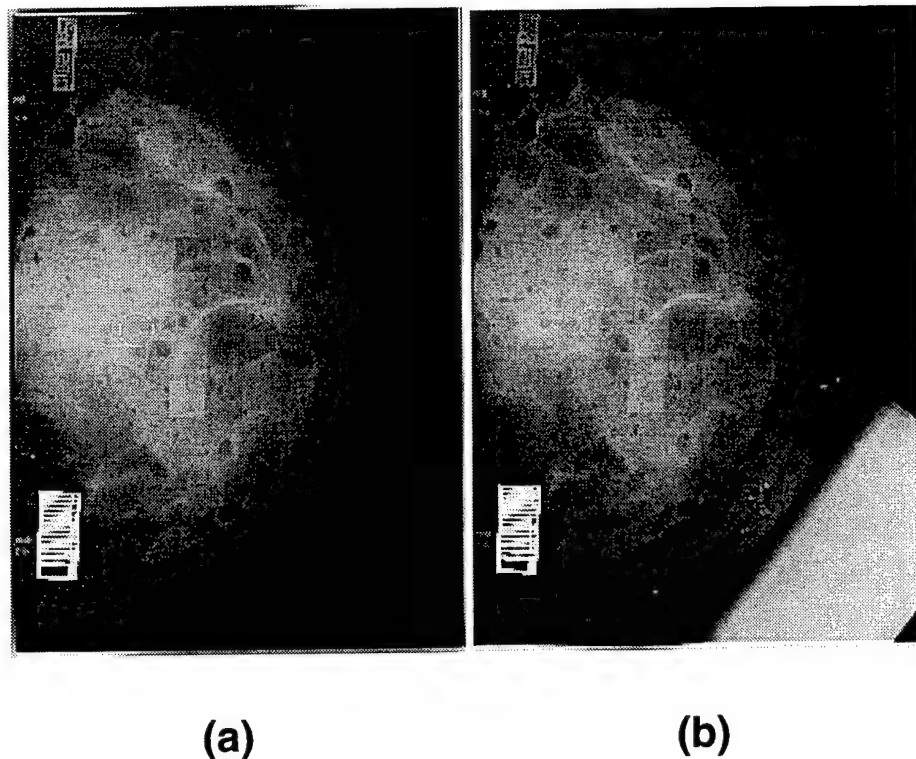
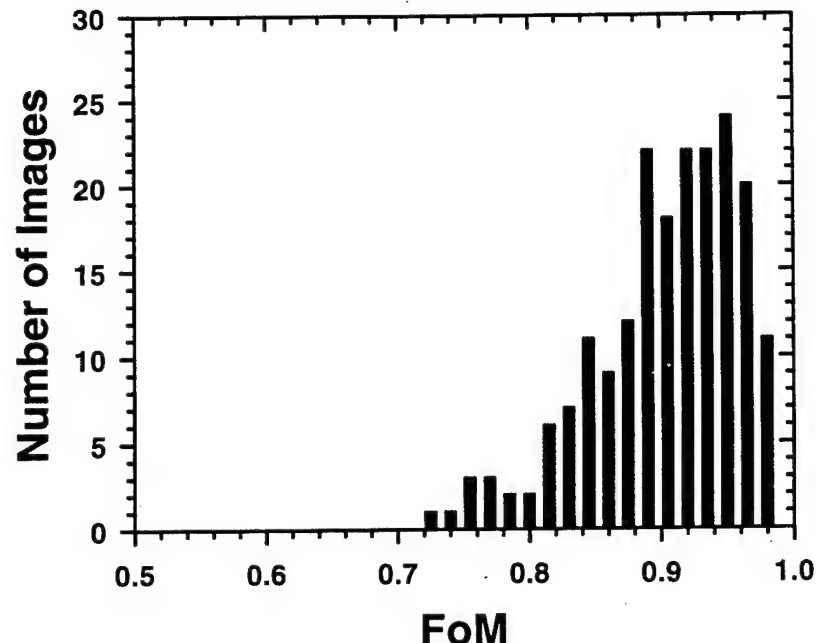
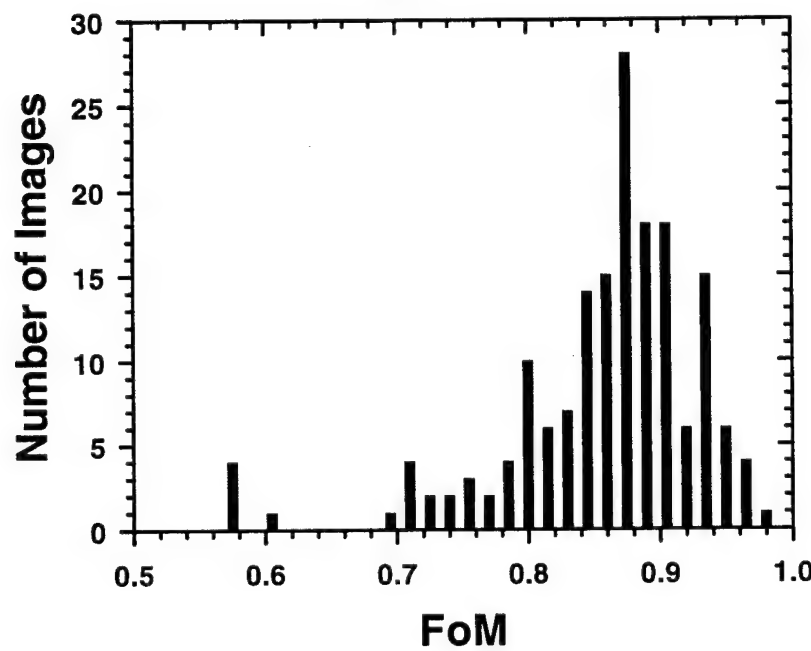


Figure 10. CIRS phantom image (a) unequalized and (b) equalized with a solid filter made with Teflon. A piece of silly putty was placed on top of the phantom to simulate dense breast parenchyma and calcium carbonate specks were placed at the periphery. The visibility of the peripheral region of the dense parenchyma and of the breast phantom is improved by equalization.



(a)



(b)

Figure 11. Distribution of the Figure-of-Merit for the group of (a) CC-view and (b) MLO view images.

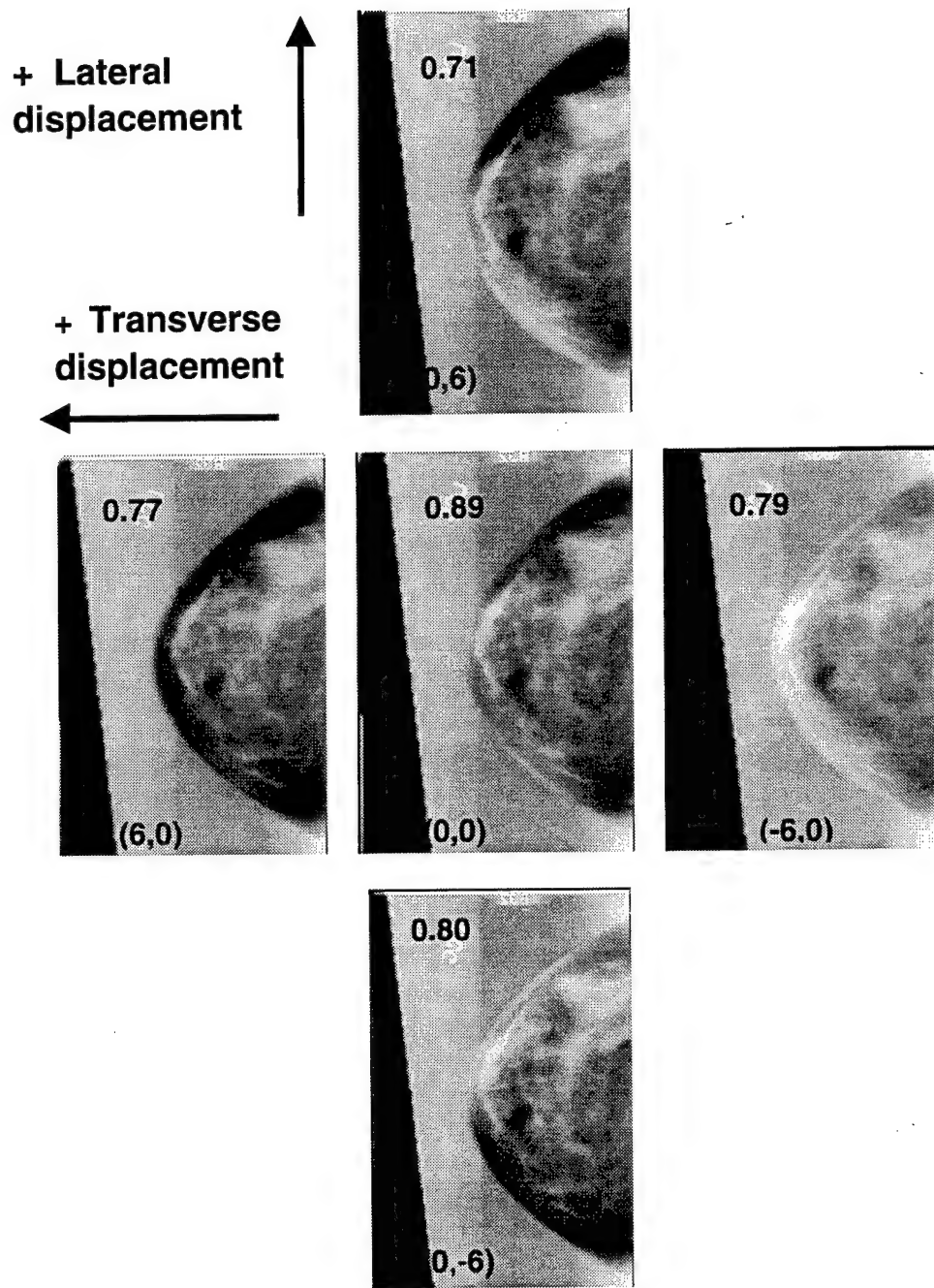
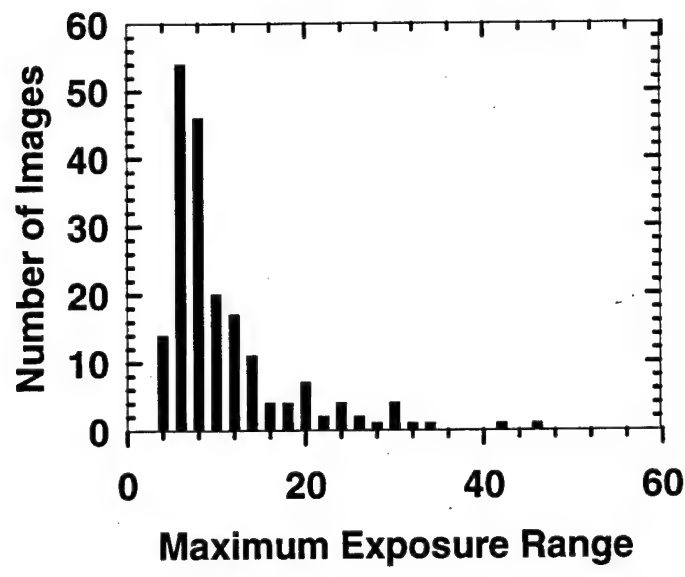
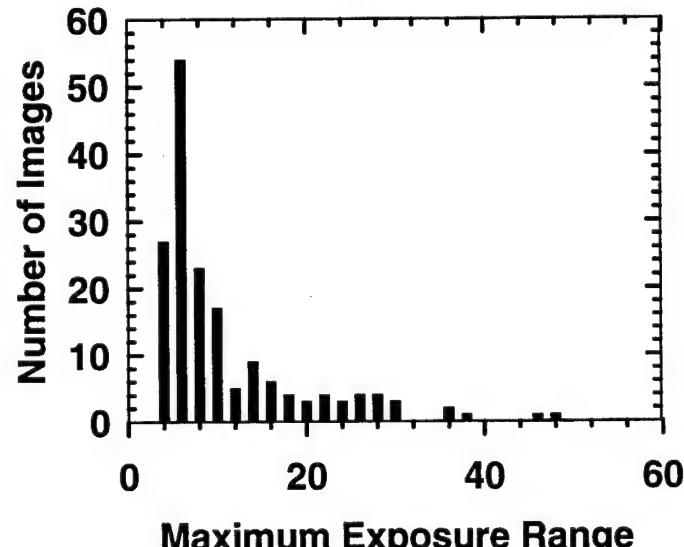


Figure 12. Effect of filter misalignment on the FoM. The dark areas seen along the breast periphery are due to under-compensation whereas the lighter areas are due to over-compensation. The numbers in parentheses indicate the filter displacements and the numbers at the upper left corner are the corresponding FoM values.

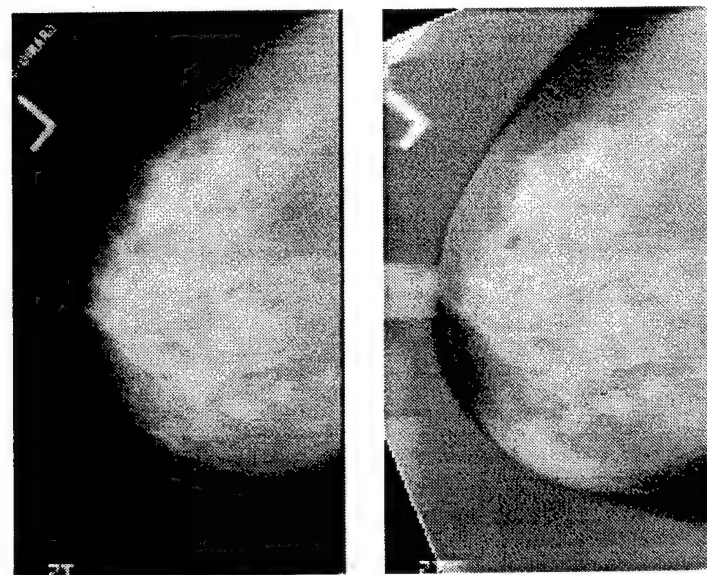


(a)

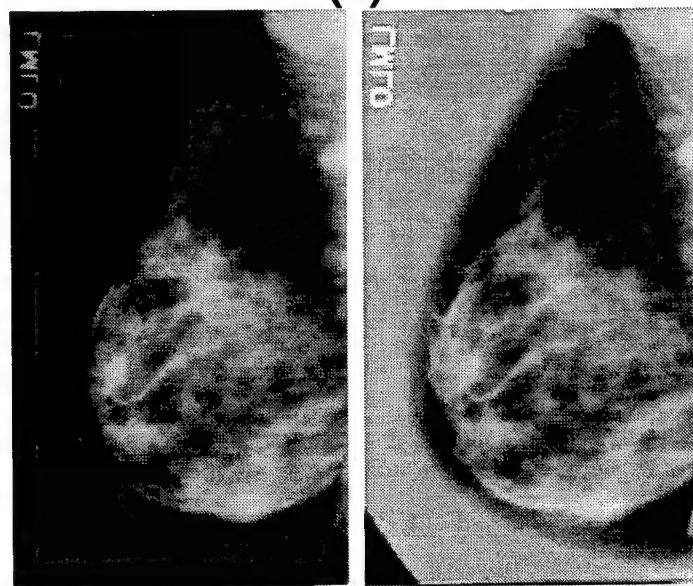


(b)

Figure 13. Histogram of maximum exposure range for the group of (a) CC-view and (b) MLO-view images.



(a)



(b)

Figure 14. Example of images with artifacts: (a) unequalsized CC-view image (left) and equalsized image with under-compensation artifact (right) in the upper portion and below the nipple, (b) unequalsized MLO-view image (left) and equalsized image with over-compensation artifact (right) in the lower portion of the breast periphery.

Classification of compressed breast shapes for the design of equalization filters in x-ray mammography

Mitchell M. Goodsitt,^{a)} Heang-Ping Chan, Bob Liu,^{b)} Shankar V. Guru,^{c)} A. Ray Morton,^{d)} Shyam Keshavmurthy, and Nick Petrick

Department of Radiology, University of Michigan Hospital, Ann Arbor, Michigan 48109

(Received 28 May 1997; accepted for publication 17 March 1998)

We are developing an external filter method for equalizing the x-ray exposure in mammography. Each filter is specially designed to match the shape of the compressed breast border and to preferentially attenuate the x-ray beam in the peripheral region of the breast. To be practical, this method should require the use of only a limited number of custom built filters. It is hypothesized that this would be possible if compressed breasts can be classified into a finite number of shapes. A study was performed to determine the number of shapes. Based on the parabolic appearances of the outer borders of compressed breasts in mammograms, the borders were fit with the polynomial equations $y = ax^2 + bx^3$ and $y = ax^2 + bx^3 + cx^4$. The goodness-of-fit of these equations was compared. The a, b and a, b, c coefficients were employed in a K-Means clustering procedure to classify 470 CC-view and 484 MLO-view borders into 2–10 clusters. The mean coefficients of the borders within a given cluster defined the “filter” shape, and the individual borders were translated and rotated to best match that filter shape. The average rms differences between the individual borders and the “filter” were computed as were the standard deviations of those differences. The optimally shifted and rotated borders were refit with the above polynomial equations, and plotted for visual evaluation of clustering success. Both polynomial fits were adequate with rms errors of about 2 mm for the 2-coefficient equation, and about 1 mm for the 3-coefficient equation. Although the fits to the original borders were superior for the 3-coefficient equation, the matches to the “filter” borders determined by clustering were not significantly improved. A variety of modified clustering methods were developed and utilized, but none produced major improvements in clustering. Results indicate that 3 or 4 filter shapes may be adequate for each mammographic projection (CC- and MLO-view). To account for the wide variations in exposures observed at the peripheral regions of breasts classified to be of a particular shape, it may be necessary to employ different filters for thin, medium and thick breasts. Even with this added requirement, it should be possible to use a small number of filters as desired. © 1998 American Association of Physicists in Medicine. [S0094-2405(98)00106-0]

Key words: mammography, equalization, classification, filtration

I. INTRODUCTION

Mammographic abnormalities related to early breast cancers include clustered microcalcifications, spiculated and irregular masses, areas of parenchymal distortion, and skin thickening.^{1,2} These abnormalities are often subtle and low contrast. Therefore, low-energy radiation and high-contrast screen/film systems are recommended for mammographic imaging in order to increase the contrast between the lesion and the background tissue. Despite the use of vigorous compression during examinations,³ the low-energy x-ray beam results in a wide dynamic range (the ratio of the maximum to the minimum x-ray exposure at the detector) for the radiation penetrating the breast. This range can be greater than 100.⁴ On the other hand, high-contrast film provides a narrow latitude which is about 10 for a typical mammographic system.^{5,6} As a result, thick and glandular regions of the breast are often imaged at the toe of the sigmoid-shaped sensitometric curve of the screen/film system; whereas thin peripheral regions are imaged at the shoulder. The contrast

and signal-to-noise ratio (SNR) of mammographic features are greatly reduced in these regions due to decreased film gradient. The contrast sensitivity of the human visual system also drops rapidly as the film density increases.^{7–9} Kopans¹⁰ found that 70% of breast cancers in women with dense breasts are in the periphery of the mammary parenchyma adjacent to the subcutaneous fat or retromammary fat. The poor image quality in the peripheral region thus imposes a serious limitation on the sensitivity of cancer detection in breasts with dense fibroglandular tissue.

A variety of exposure equalization methods have been proposed to improve mammographic imaging. In one, either a water bag^{11–13} or a solid, elastic, unit density x-ray attenuator¹⁴ is placed between the breast and the compression paddle to make the total breast thickness uniform all the way out to the periphery. This gap-filling method has the advantage of being patient specific. However, it can be difficult to implement, especially for oblique views. Another, more sophisticated method involves scanning of the breast

with either single or multiple x-ray beams that are intensity modulated based on x-ray transmission signals obtained from single or multiple detectors.^{15,16} Such a method can equalize the exposure throughout the breast rather than just at the periphery. However, the method is complex and requires much greater heat loading of the x-ray tube than conventional mammography. Recently, a rotary scanning equalization method has been developed that reduces, but does not eliminate the heat loading and complexity issues.¹⁷

We have proposed a practical and cost-effective exposure equalization method for reducing the dynamic range of the mammograms. The method employs a set of x-ray beam intensity shaping filters that are positioned near the collimator of the mammography system. Each filter is designed to match the shape of the compressed breast border and to preferentially reduce the exposure to the detector in the peripheral region of the breast. It is our hypothesis that compressed breasts can be classified into a finite number of shapes, and therefore only a finite number of filters will be needed. In this paper, we report on the results of a study we conducted to determine the validity of our hypothesis.

II. METHODS

A. Border detection and modelling

1004 clinical mammograms including both craniocaudal (CC) and mediolateral oblique (MLO) views were digitized with a DBA Systems, Inc. (Melbourne, Florida) model ImageClear M2100 film digitizer. This system has 21 micron resolution, which is much finer than is required for our application. We operated the digitizer in a mode whereby two of every three pixels is skipped, yielding an effective resolution of 63 microns. The resolution was further reduced to 1 mm by averaging the pixel values in 1 mm areas. The light transmission through the films was digitized in 16-bit linear format, and these values were later converted to 12-bit logarithmic format to yield a fairly linear relationship between film optical density and digitized value.

An automated border tracing algorithm was applied to the digitized images.¹⁸ Acceptable borders were obtained in 95% of the mammograms (954 of the 1004), which formed the data set used in our study. The 5% of the mammograms that were excluded exhibited problems such as: (1) a substantial portion of the breast edge extended outside the imaging area of the film; (2) a significant portion of the breast edge was obscured by a patient label; and (3) numerous artifacts (e.g., streaks) were present at the breast periphery caused by the film digitizer. In a separate study, we found the automated border trace routine to be accurate. Comparing the difference between hand-traced and automatically detected borders in a random sample of images, we computed an average root-mean-square difference of 1.4 mm (1.4 pixels).¹⁹ An example of the manually traced and automatically detected borders is shown in Fig. 1.

A total of 470 CC-view and 484 MLO-view automatically traced borders were analyzed in the present study. In reviewing these borders, we observed that the shapes appear to be well characterized by either symmetric or asymmetric poly-

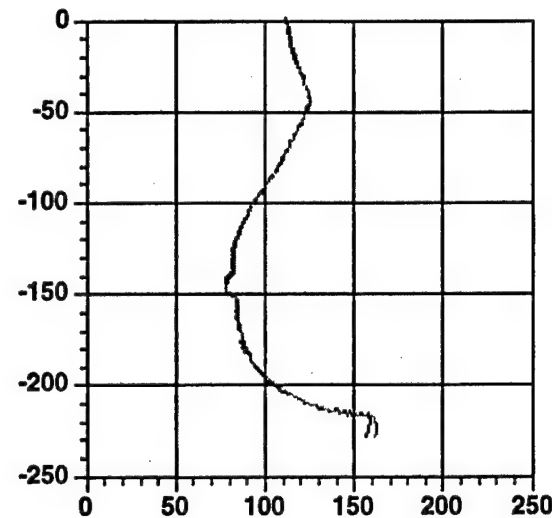


FIG. 1. Example of automatic versus hand-traced compressed breast borders. The hand-traced border is indicated by the lighter gray curve.

nomials. Therefore, we decided to model the borders with the polynomial equations $y = ax^2 + bx^3$ and $y = ax^2 + bx^3 + cx^4$. These equations have the advantage of producing only two (a, b) or three (a, b , and c) coefficients which can be used in cluster analysis to classify the border shapes.

B. The border fitting procedure

The fitting procedure involves either translating and rotating the borders about the x - and y -axes or, equivalently, translating and rotating the axes. We wrote custom software to accomplish this task. The method is described below.

First, small irregularities are removed from the borders by applying run-length averaging (run-length employed = 15).

Next, an initial best estimate of the axis positions is made. The approach that was utilized is illustrated in Fig. 2. In brief, it determines the y' -axis by least-square fitting a line

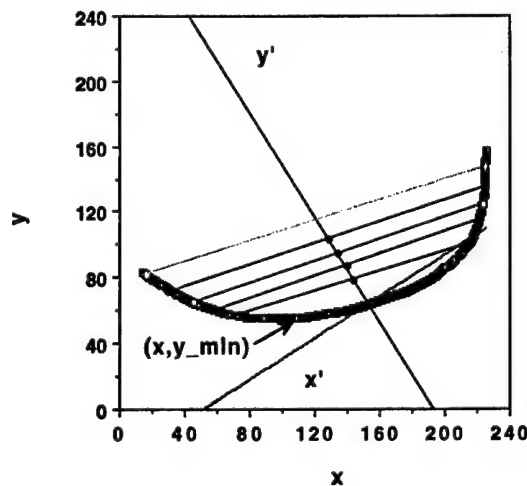


FIG. 2. Example of the x' - y' starting axes computed with the subroutine STARTAXIS. These axes are translated and rotated to find the best fits to the borders using the equations $y' = ax'^2 + bx'^3$ and $y' = ax'^2 + bx'^3 + cx'^4$.

through the midpoints of line segments drawn between appropriate points on the right and left sides of the borders. When suitable line segments are drawn, the border will be fairly symmetric about the line through the midpoints of the line segments, and this line should be a good starting axis for the curve fits.

The algorithm that was written to locate the initial axes, STARTAXIS, first determines the point on the border that has a minimum y -value, (x, y_{min}) . Next, the number of points on the border to the left and right of (x, y_{min}) are computed. If either number is less than 25, the topmost point on that side is selected as a starting point. Otherwise, the derivatives (dy/dx) of the topmost 25% of the points on each side of (x, y_{min}) are computed. The point at which the derivative is a minimum (most negative) on the left side of (x, y_{min}) is selected as a starting point for the left side. Similarly, the point at which the derivative is a maximum (most positive) on the right side is selected as the starting point for the right side. (The topmost, light gray line in Fig. 2 connects the left and right starting points.) Next, the number of points between the left starting point and (x, y_{min}) , and the number of points between the right starting point and (x, y_{min}) are computed. The smaller of these two numbers is divided by 5 to create an incremental unit. Using the convention that the endpoint of the border on the left is point number 1 and the endpoint on the right is the final point, line segments are determined between points on the border corresponding with the leftmost starting point plus an integer multiple of the incremental unit and the rightmost starting point minus that same value. (See the black lines in Fig. 2) Finally, the midpoint of each line segment is computed.

The y' -axis is then ascertained by least square fitting a line between the midpoints of the line segments. The intersection of this line with the border is defined to be the origin, and the x' axis is the line perpendicular to the y' -axis passing through the origin (see Fig. 2).

C. Determination of best fit by translation and rotation of axes to find the best fit

The next task of the computer program is the translation and rotation of the axes to find the best fit of the polynomial equation to the smoothed border. Equations employed for the translation and rotation were:

$$x' = x_s \cos \theta + y_s \sin \theta$$

and

$$y' = -x_s \sin \theta + y_s \cos \theta,$$

where $x_s = x - x_{\text{origin}} + x_{\text{shift}}$, $y_s = y - y_{\text{origin}} + y_{\text{shift}}$, and $\theta = (\pi/180) \cdot (\theta_{\text{Start}} + \theta_{\text{shift}})$. $(x_{\text{origin}}, y_{\text{origin}})$ and θ_{Start} are the coordinates of the origin and the angle of the starting abscissa (in degrees relative to the x -axis), respectively, and x_{shift} , y_{shift} , and θ_{shift} are the translation and rotation values.

The fit error was defined to be the root-mean-square (rms) distance between corresponding y -values on the smoothed, automatically detected borders and the fitted borders. The equation utilized was

$$\text{error} = \sqrt{\sum_{i=1}^n (y_i - y_{\text{fit}_i})^2 / n}.$$

The best fit corresponded to a minimum rms error.

To improve the efficiency of this process, we first employ coarse shifts and rotations with increments of 4 mm and 4 degrees, respectively. We use an x -translation range of $+/- 40$ mm, a y -translation range of $+/- 20$ mm and rotation angle range of $+/- 40$ degrees. The translation shifts $(x_{\text{shift}}, y_{\text{shift}})$ and the angle shift (θ_{shift}) corresponding to the best fit are found. After this, finer increments of 1 mm and 1 degree are employed within the best "coarse" shift ranges $+/- 4$ mm and $+/- 4$ degrees. For each type of fit ($y = ax^2 + bx^3$ and $y = ax^2 + bx^3 + cx^4$), the entire fitting and shifting iteration process takes about $\frac{1}{2}$ second per border on a Digital Equipment Corporation (DEC) AlphaStation. The validity of the above chosen ranges is confirmed by the fact that the fits within these ranges had average rms errors of about 2 mm or less and only in very rare instances (11 cases for CC and 24 for MLO including both a, b and a, b, c fits) did the best fit occur at the limits of translation or rotation. Furthermore, in the majority of the latter cases (e.g., 32 of 35 cases), the fit errors were less than 2.5 mm, which is considered a very good fit.

Finally, to verify that the minima in the rms fit errors were not passed over using coarse followed by fine increments in translation and angulation, the computation was repeated in 229 cases using only fine increments. The resulting rms fit errors were on the average only 0.01 less than those using coarse followed by fine increments, the rms difference between the errors was only 0.02, and the maximum rms difference was 0.13. Thus in general, the minima were not passed over, and greater efficiency was achieved without sacrificing accuracy.

D. Cluster analysis

To classify the border shapes, the resulting best fit coefficients (either a and b or a, b , and c) for each border were introduced into a K-Means Cluster Analysis algorithm incorporated in the SPSS statistical package (SPSS Inc., Chicago, IL). This clustering method is based upon nearest neighbor sorting, whereby each case is assigned to the cluster for which the distance between the cluster center and the case is a minimum.²⁰ Since the cluster centers are not known initially, they are iteratively estimated from the data. The coefficients for the CC-view and MLO-view borders were analyzed separately. Absolute values of the b -coefficients were used since the curve shapes for positive and negative b -values are mirror images of one another. Thus the same filter could be employed; it would simply have to be flipped 180 degrees for one of the b -value polarities. We used the K-Means method to classify the borders into 2, 3, 4, 5, 6, 8, and 10 clusters.

In addition, we performed limited studies of various modifications of traditional K-Means clustering. In one, which we termed the "hybrid technique," the a and b parameters were employed (c set to 0) when the fit to a given

border using $y = ax^2 + bx^3$ was better than a threshold value (e.g., when the rms error was ≤ 3 mm (3 pixels)). Otherwise, the border was refit using $y = ax^2 + bx^3 + cx^4$, and the a , b , and c parameters of that fit were employed. This hybrid method is based on the assumption that if the fit to the 2-parameter equation is sufficient, it is not necessary to use a 3-parameter fit. It is further assumed that under those circumstances, use of the coefficient (c) of the fourth order term only adds noise to the data being clustered.

In a second modification, we used the Z-scores of the variables (a , b , and c) rather than the variables themselves in the cluster analysis. The Z-score is the number of standard deviations that a given variable for a particular border differs from the mean value for all borders. Such a method makes the importance of each parameter more equivalent. It compensates for the wide variations in the magnitudes of the parameters. For example, the b -values were about 20 to 200 times smaller than the a -values, and the c -values were about 20 to 500 times smaller than the b -values.

Finally, in a third modification, we first applied K-Means Cluster analysis to the entire CC border set to obtain six clusters. We then fixed the cluster membership for the two best clusters, eliminated the corresponding borders from the data set, and performed K-Means Cluster analysis on the remaining borders. The second stage cluster analysis classified the remaining borders into 4, 5, or 6 clusters. The resulting total number of clusters was 6, 7, or 8, respectively. The underlying assumption for this method was that better clustering might be obtained in the second stage for the smaller set of borders. Thus, the overall clustering would be better than when the entire set of borders was clustered all at one time.

E. Determination of filter shapes and refitting of borders

Once the classification of each border was determined, the mean a and b values or mean a , b , and c values for the borders within each class were determined. The border defined by the equation using the mean coefficients defined the "filter." A computer routine was written to translate and rotate each of the individual borders within each class to best match their corresponding "filter." This routine again utilized coarse and fine increments for translation and rotation similar to the increments employed in the original fitting routine. The translation and rotation values determined with the original fitting routine were employed as starting values for the matching routine. The rms distance between the individual border and the filter of its class was minimized as an indication of best match. For each filter or class, the mean and standard deviation of the rms distances were computed. These values were used to quantitatively assess the success of the border classification. Also, for each type of clustering, the overall mean rms distance for all of the filters was computed using the equation:

$$\bar{d} = \sum_{g=1}^N \sum_{i=1}^{P_g} \text{rms}_{ig}/T,$$

where N is the total number of clusters (e.g., 2, 3, 4, 5, 6, 7, 8 or 10), P_g is the number of borders in cluster g , rms_{ig} is the rms distance between border i and the filter for cluster g , and T is the total number of borders (e.g., $T = \sum_{g=1}^N P_g$). In addition, a figure of merit (FOM) was derived to estimate the optimal number of clusters. The equation employed was

$$\text{FOM} = \sum_{g=1}^N (P_g / (\overline{\text{rms}}_g)^2) / \sqrt{N},$$

where P_g and N are as defined above, and $\overline{\text{rms}}_g$ is the average rms error for cluster g . The denominator in this equation (\sqrt{N}) is a term that penalizes the use of larger numbers of clusters, and the numerator gives greater weight to those clusters having greater number of borders and smaller rms errors. Finally, the newly rotated and translated borders were refit with the equations $y = ax^2 + bx^3$ and $y = ax^2 + bx^3 + cx^4$. The new coefficients, (a, b) and (a, b, c) , were plotted to enable visual evaluation of the success of classification.

F. Investigation of optical density and exposure values near the filter position

The filters that will eventually be built must be custom-shaped in the thickness dimension to compensate for the variations in x-ray transmission at the periphery of the breast. To assess this effect, we computed mean optical density and mean exposure profiles along normals to the "filter" contour for one of the highly populated clusters in the classification study of CC-view mammograms. The particular cluster consisted of 231 of the 470 CC-view borders, and it was computed by the K-Means technique for the case in which there was a total of six clusters, and the borders were fit with the equation $y = ax^2 + bx^3$. Twenty-one equally spaced normals were derived along the contour of the "filter." Each normal started at a position about 1 cm outside the "filter" contour and extended about 2 cm inside the contour (into the breast). The pixel values at the points along the normals were converted to optical densities using a pixel value to optical density transform derived from the film digitizer calibration curve. The means and standard deviations of the optical densities along each normal were computed. To convert the optical densities to x-ray exposures, which would eventually be needed for the filter design, we derived a film characteristic curve using x-ray sensitometry. The curve was generated with a bootstrap method using three mAs values (2, 20, and 100), four focus-to-film distances (23.5, 33.5, 47.5, and 66.5 cm), and three Lucite attenuator thicknesses (12, 24, and 36 mm). Within each segment, the four distances were employed at fixed mAs and fixed attenuator thickness. This was done to avoid errors due to reciprocity law failure and due to changes in x-ray beam quality. The curve segments were then bootstrapped together to create a characteristic curve extending over the entire exposure range. All measurements were made at 28 kVp, which is typical for the wide range of mammograms analyzed in this study. A

TABLE I. Results of fitting the CC- and MLO-view borders with the equations $y = ax^2 + bx^3$ and $y = ax^2 + bx^3 + cx^4$.

No. of images	View	Type of fit	Mean rms error between fit and run-length averaged automatically tracked border (mm)
470	CC	a, b	2.18
470	CC	a, b, c	1.07
484	MLO	a, b	1.53
484	MLO	a, b, c	1.07

Keithley (Cleveland, Ohio) model 35050A dosimeter with a Keithley model 96035 15-cc ionization chamber was used to measure the exposures at the closest position, and the exposures at other positions were computed using the inverse square law.

III. RESULTS

The average rms errors for the fitting of the original run-length averaged borders with the equations $y = ax^2 + bx^3$ and $y = ax^2 + bx^3 + cx^4$ are compared in Table I. The data in the fourth column of this table demonstrate that both fits are very good [errors are ~ 2 mm (pixels) or less], and use of 3-coefficients (a, b, c) reduced the fitting errors by about 30%–50%. An example of a fitted curve for which the rms error is equal to the mean value for all MLO views (1.53 mm) using the a and b parameters is displayed in Fig. 3, below. Figure 4 illustrates a case in which the rms error was 4.03 mm for the two parameter (a, b) fit and 1.18 mm for the three parameter (a, b, c) fit.

Clustering results are listed in Tables II to IV. The mean rms distances or errors between individual borders within clusters and their corresponding “filters” for CC-view borders are listed in Table II and those for the MLO-view bor-

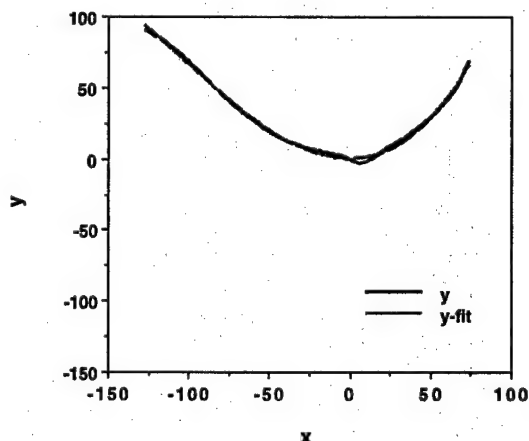
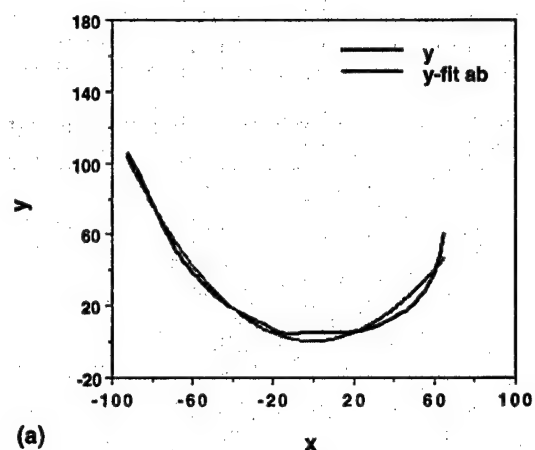
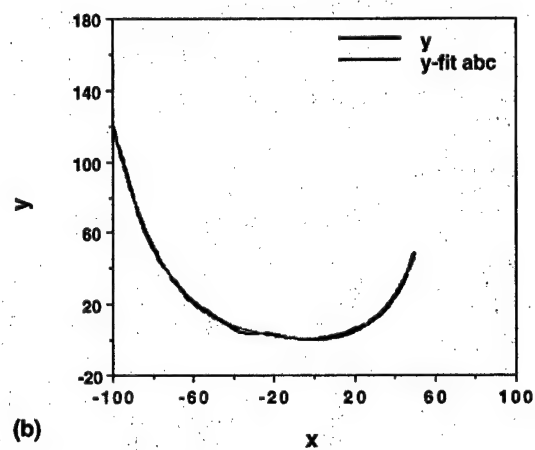


FIG. 3. Example of a fit for an MLO-view in which the fitted border (lighter curve) has an rms error of 1.53 mm, which is equal to the mean value for all MLO-views obtained using the a - and b -parameter fitting routine.



(a)



(b)

FIG. 4. Example of a case in which a fitted border using the 3-coefficient (a, b, c) equation is significantly superior to that using the 2-coefficient (a, b) equation. The same MLO-view border was fit using both equations. The rms error for the 2-coefficient fit (part a) is 4.03 mm and that for the 3-coefficient fit (part b) is 1.18 mm.

ders are listed in Table III. The overall mean rms distances between the borders and filters for the various clustering parameters and methods are listed in Table IV.

Scattergrams displaying the original a and b fitting coefficients for the 470 CC-view borders and 484 MLO-view borders are shown in Fig. 5. These are the a and b values that are input into the K-Means Cluster analysis program. Figure 6 shows examples of the a and b and a, b , and c values of the second-stage fits to the borders after they were translated and rotated to best match the cluster “filter” (the curve generated with the mean coefficients for the cluster).

Our clustering figure of merit as a function of number of clusters is plotted in Fig. 7.

Figure 8 shows an overlay of a “filter” and its associated normals on a mammogram whose automatically traced breast border was clustered to belong to the filter shape. Examples of filter shapes for the CC- and MLO-views are illustrated in Fig. 9(a) and (b), respectively.

Finally, plots of the mean film optical densities as a function of position along normals to the “filter” are shown in Fig. 10(a) and (b). As described in the Materials and Methods section, the mean values were obtained from the 231

TABLE II. Mean rms distances (mm) between individual borders and "filters" for CC-views. (Standard deviations for each distribution are noted in parentheses.) Results in each row are ordered from the smallest mean rms distance to the largest. n = number of borders in a particular cluster.

(A). a, b fit		Cluster									
		1	2	3	4	5	6	7	8	9	10
2		2.7 (1.4)	3.7 (2.1)								
	$n=314$	$n=156$									
3		2.2 (1.2)	2.6 (1.2)	4.1 (2.4)							
	$n=139$	$n=248$	$n=83$								
4		2.0 (1.1)	2.4 (1.1)	3.5 (4.0)	3.6 (2.0)						
	$n=93$	$n=235$	$n=9$	$n=133$							
5		2.1 (1.1)	2.5 (1.2)	3.5 (4.1)	3.7 (2.7)	3.8 (2.1)					
	$n=137$	$n=232$	$n=9$	$n=4$	$n=88$						
6		2.1 (1.1)	2.5 (1.2)	3.1 (3.3)	3.7 (2.7)	3.7 (2.1)	3.9 (6.1)				
	$n=131$	$n=231$	$n=5$	$n=4$	$n=95$	$n=4$					
6 (2 best from 6 clusters + recluster remaining into 4 clusters)		2.1 (1.1)	2.5 (1.2)	3.4 (2.1)	3.5 (4.1)	3.7 (2.7)	3.8 (2.1)				
	$n=131$	$n=231$	$n=60$	$n=9$	$n=4$	$n=35$					
7 (2 best from 6 clusters + recluster remaining into 5 clusters)		2.1 (1.1)	2.5 (1.2)	3.4 (2.1)	3.4 (2.9)	3.5 (4.1)	3.8 (2.0)	3.8 (2.9)			
	$n=131$	$n=231$	$n=60$	$n=2$	$n=9$	$n=35$	$n=2$				
8 (2 best from 6 clusters + recluster remaining into 6 clusters)		2.1 (1.1)	2.5 (1.2)	3.1 (3.3)	3.4 (2.2)	3.4 (2.9)	3.7 (1.9)	3.8 (2.9)	3.9 (6.1)		
	$n=131$	$n=231$	$n=5$	$n=55$	$n=2$	$n=40$	$n=2$	$n=2$	$n=4$		
8		1.7 (0.9)	2.0 (0.9)	2.3 (1.2)	3.0 (1.7)	3.1 (3.3)	3.7 (2.7)	3.8 (2.3)	3.9 (6.1)		
	$n=52$	$n=119$	$n=144$	$n=93$	$n=5$	$n=4$	$n=49$	$n=4$			
10		0.9 (0)	1.7 (0.9)	2.0 (0.9)	2.3 (1.2)	2.8 (1.5)	3.2 (3.1)	3.4 (2.9)	3.8 (2.9)	3.9 (2.3)	3.9 (6.1)
	$n=1$	$n=52$	$n=113$	$n=145$	$n=89$	$n=4$	$n=2$	$n=2$	$n=58$	$n=4$	
(B). a, b, c fit		Cluster									
		1	2	3	4	5	6	7	8	9	10
2		2.9 (1.7)	3.1 (2.0)								
	$n=82$	$n=388$									
3		2.8 (1.7)	3.2 (2.0)	3.2 (2.1)							
	$n=175$	$n=23$	$n=272$								
4		2.7 (1.8)	2.9 (1.9)	3.2 (2.0)	3.6 (2.2)						
	$n=205$	$n=60$	$n=199$	$n=6$							
5		2.4 (1.4)	2.7 (1.7)	3.0 (2.0)	3.6 (2.4)	3.6 (2.2)					
	$n=34$	$n=136$	$n=202$	$n=92$	$n=6$						
6		1.0 (0.0)	2.4 (1.4)	2.7 (1.7)	2.9 (2.2)	3.0 (2.0)	3.6 (2.4)				
	$n=1$	$n=34$	$n=136$	$n=5$	$n=204$	$n=5$	$n=90$				
6 hybrid ^a		1.7 (2.0)	2.0 (1.1)	2.2 (0.7)	2.3 (1.9)	4.2 (2.8)	4.5 (2.8)				
	$n=7$	$n=157$	$n=48$	$n=139$	$n=80$	$n=44$					
6 using Z-scores		1.0 (0.0)	1.3 (0.8)	1.4 (0.0)	2.6 (1.6)	3.1 (2.0)	4.4 (4.1)				
	$n=1$	$n=2$	$n=1$	$n=136$	$n=309$	$n=21$					
8		1.0 (0.0)	1.3 (0.0)	1.8 (1.0)	2.4 (1.5)	2.7 (1.6)	2.8 (2.0)	3.0 (1.8)	4.0 (2.7)		
	$n=1$	$n=1$	$n=4$	$n=28$	$n=109$	$n=130$	$n=145$	$n=52$	$n=52$		
8 hybrid ^a		0.8 (0.1)	1.9 (1.8)	2.0 (1.1)	2.1 (1.5)	2.2 (0.6)	3.7 (2.2)	4.1 (3.8)	4.6 (3.0)		
	$n=3$	$n=4$	$n=4$	$n=140$	$n=134$	$n=44$	$n=52$	$n=66$	$n=27$		
10		0.7 (0.0)	1.0 (0.0)	1.3 (0.0)	2.1 (1.0)	2.4 (1.5)	2.7 (1.6)	2.8 (2.0)	2.9 (1.7)	3.1 (2.0)	4.2 (2.8)
	$n=1$	$n=1$	$n=1$	$n=3$	$n=28$	$n=103$	$n=107$	$n=122$	$n=72$	$n=32$	

^aHybrid=use a, b coefficients ($c=0$) when original fit error ≤ 3.0 mm, use a, b, c coefficients when original fit error > 3.0 mm.

TABLE III. Mean rms distances (mm) between individual borders and "filters" for MLO-views. (Standard deviations for each distribution are noted in parentheses.) Results in each row are ordered from the smallest mean rms distance to the largest. n = number of borders in a particular cluster.

(A). a, b fit

Total no. of clusters	Cluster									
	1	2	3	4	5	6	7	8	9	10
2	2.2 (1.1) $n=306$	3.2 (1.9) $n=178$								
3	1.9 (0.9) $n=172$	2.2 (1.1) $n=227$	3.5 (2.0) $n=85$							
4	1.7 (0.7) $n=107$	1.9 (0.8) $n=219$	2.9 (1.4) $n=134$	4.1 (1.9) $n=24$						
5	1.7 (0.7) $n=154$	1.8 (0.8) $n=58$	2.2 (1.1) $n=185$	3.4 (1.8) $n=83$	4.0 (3.1) $n=4$					
6	1.6 (0.7) $n=109$	1.9 (0.8) $n=179$	2.1 (0.7) $n=18$	2.5 (1.3) $n=129$	3.3 (3.1) $n=3$	3.7 (1.9) $n=46$				
8	0.6 (0.0) $n=1$	0.8 (0.0) $n=1$	1.6 (0.7) $n=142$	1.8 (0.8) $n=64$	2.0 (0.8) $n=165$	3.0 (1.4) $n=87$	4.0 (2.0) $n=22$	4.0 (3.2) $n=2$		
10	0.6 (0.0) $n=1$	0.8 (0.0) $n=1$	1.5 (0.6) $n=81$	1.5 (0.0) $n=1$	1.7 (0.7) $n=117$	1.9 (0.8) $n=150$	2.1 (0.7) $n=17$	2.8 (1.4) $n=71$	3.3 (1.6) $n=35$	4.8 (2.3) $n=10$

(B). a, b, c fit

Total no. of clusters	Cluster									
	1	2	3	4	5	6	7	8	9	10
2	2.9 (2.2) $n=191$	3.6 (2.3) $n=293$								
3	2.7 (2.3) $n=234$	3.1 (1.9) $n=81$	3.9 (2.4) $n=169$							
4	2.9 (2.2) $n=229$	2.9 (2.2) $n=123$	4.0 (2.5) $n=130$	6.4 (1.6) $n=2$						
5	2.4 (1.9) $n=188$	3.0 (2.3) $n=81$	3.2 (2.2) $n=153$	4.9 (3.0) $n=60$	6.4 (1.6) $n=2$					
6	2.3 (2.1) $n=140$	2.9 (1.8) $n=71$	3.3 (2.4) $n=147$	3.7 (2.3) $n=111$	4.8 (3.3) $n=13$	6.4 (1.6) $n=2$				
6	1.5 (0.3) $n=2$	2.1 (1.5) $n=138$	2.4 (2.4) $n=152$	2.6 (1.1) $n=65$	3.3 (3.0) $n=106$	5.5 (4.8) $n=21$				
8	0.3 (0.0) $n=1$	1.3 (0.0) $n=1$	2.6 (2.0) $n=127$	2.6 (1.4) $n=53$	2.7 (2.7) $n=76$	3.3 (2.3) $n=115$	3.7 (2.4) $n=98$	4.8 (3.3) $n=13$		
10	0.3 (0.0) $n=1$	1.3 (0.0) $n=1$	2.4 (2.4) $n=78$	2.8 (2.0) $n=114$	2.8 (1.0) $n=13$	3.2 (1.5) $n=28$	3.4 (2.0) $n=76$	3.5 (2.4) $n=97$	4.9 (3.2) $n=7$	4.9 (3.4) $n=41$

^aHybrid=use a, b coefficients ($c=0$) when original fit error ≤ 3.0 mm, use a, b, c coefficients when original fit error > 3.0 mm.

mammograms containing compressed breast borders that were classified to belong to a particular cluster. The clustering involved 470 CC-view borders which were classified into six groups using a and b parameters. Curves depicting the mean ± 1 standard deviation for several of the normals are shown in Fig. 10(c). Figure 10(d) depicts the mean rela-

tive x-ray exposures at the film plane as a function of position along the normals.

IV. DISCUSSION

Even though the original fits are better for three coefficients (a , b , and c) instead of two (a and b) (see Table I),

TABLE IV. Overall mean rms distance between individual borders and "filters."

Total no. of clusters	Overall mean rms error (mm)			
	CC-View ab-fit	CC-View abc-fit	MLO-View ab-fit	MLO-View abc-fit
2	3.02	3.11	2.54	3.34
3	2.73	3.05	2.33	3.18
4	2.68	2.97	2.25	3.24
5	2.67	2.98	2.19	3.11
6	2.66	2.97	2.18	3.12
8	2.48	2.91	2.12	3.07
10	2.48	2.89	2.09	3.11
6 hybrid	-	2.69	-	2.68
6 using Z-scores	-	2.99	-	-
6 (2 best from 6 clusters + recluster remaining into 4 clusters)	2.63	-	-	-
7 (2 best from 6 clusters + recluster remaining into 5 clusters)	2.63	-	-	-
8 (2 best from 6 clusters + recluster remaining into 6 clusters)	2.62	-	-	-
8 hybrid	-	3.03	-	-

there is either only slight improvement [e.g., for 6 clusters in the CC case (Table II A, B)] or no improvement [for the MLO case (Table III A, B)] in the clustering success as measured by the mean rms distances between the individual borders within a class and the mean border or "filter." In fact, the overall mean rms error results listed in Table IV indicate that, in general, better matches between the individual borders and the filters are achieved when the filters are based upon the a, b clustering. Therefore, the 2-coefficient fit is preferred.

The number of filters to be employed in our exposure equalization method must be a compromise between goodness-of-fit and practicality. The results in Table IV indicate the goodness-of-fit, as represented by the overall mean rms distance error, generally improves as the number of clusters increases. However, this improvement is not very great beyond three or four clusters. The individual cluster results in Tables II and III also exhibit this trend, and the figures of merit that were derived (see Fig. 7) peak at about three clusters. Therefore, three or four filter shapes for each view appear to be optimum.

The hybrid approach of using a and b values with c set to zero when the original fit to the automatically traced border is less than or equal to a threshold value and using a , b , and c values otherwise improves the clustering relative to use of the conventional a , b , and c values in some cases (e.g., Table III B), but degrades clustering in others (e.g., Table II B). However, for all of the hybrid cases shown in the tables, the corresponding clustering that is obtained using the same total number of clusters and only the a and b parameters of the fit equation $y = ax^2 + bx^3$ yields superior results.

Use of the Z-scores of the a , b , and c values rather than the values themselves did not improve clustering (Table II B). The effect of employing the two best clusters of six from

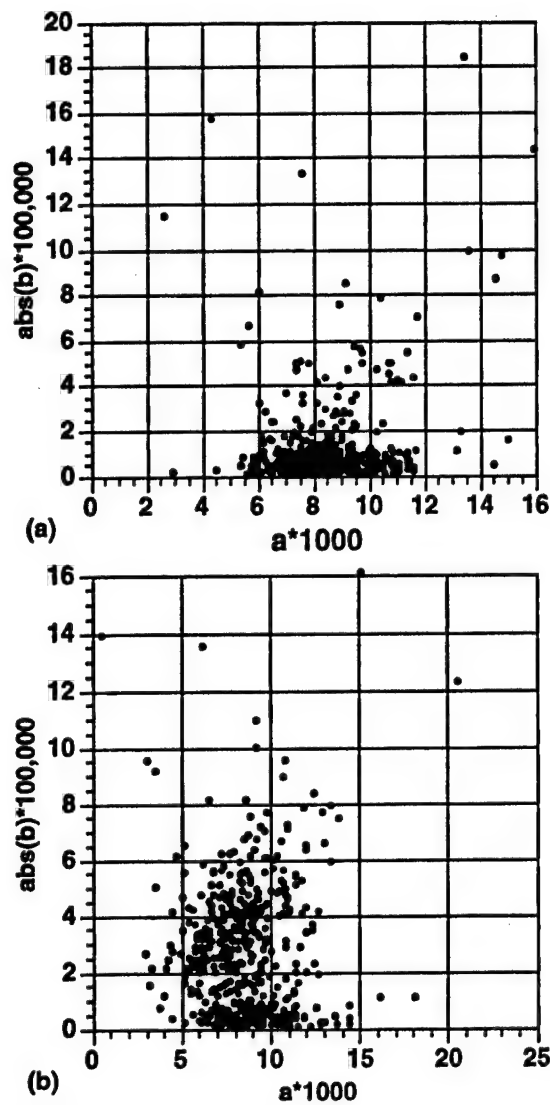


FIG. 5. Plots of a and b values of original $y = ax^2 + bx^3$ fits to borders of (a) 470 CC-view and (b) 484 MLO-view mammograms. Absolute values of b are plotted since the shapes of the curves for positive and negative b -values are mirror images of one another.

an initial cluster analysis followed by reclustering the remaining borders into 4, 5, or 6 groups was an insignificant ($\sim 1.2\% - 1.5\%$) improvement.

Figure 10(c) provides an example of the variability in the optical densities near the periphery of the breast that might be expected for a set of compressed breasts classified to be of a particular shape. The standard deviations of the optical densities range from about 0.2 to 0.6 OD. This translates to a fairly wide range of exposure values, especially in the high density region just outside the breast border. Our calculations show that, in this region, the mean exposure to the film minus 1 standard deviation is about half the mean exposure value. The mean exposure to the film plus 1 standard deviation could not be determined just outside the breast because these exposures are in the shoulder region of the film characteristic curve, where there are large uncertainties in the optical density to relative exposure conversion. Also, the op-

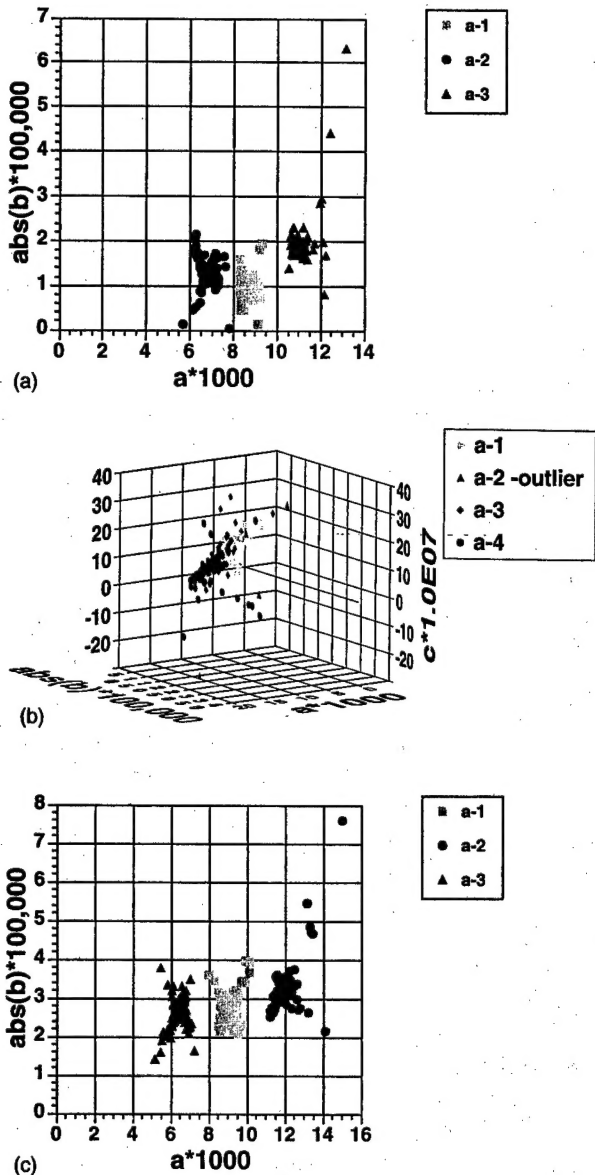


FIG. 6. Pictorial representations of clustering. The borders that are classified into each cluster are translated and rotated to best match the average border (filter) for that cluster, and they are then re-fit with the equations $y = ax^2 + bx^3$ and $y = ax^2 + bx^3 + cx^4$. The resulting a, b , or a, b , and c coefficients are plotted. Part (a) shows the a, b coefficients, and part (b) shows the a, b , and c coefficients that are generated when the 470 CC-view borders were clustered into 3-groups for a, b and 4-groups for a, b, c . (The outlier in the second group for the a, b, c clustering had $(a*1000, b*100,000, c*10^7)$ coordinates of $(5.1, 93.4, -71.7)$ and was not plotted so the other data points could be better visualized.) Part (c) shows the a, b coefficients that are generated when the 484 MLO-view borders were clustered into three groups. The particular sets shown represent the better clustering results based on the figure of merit criteria for a, b clustering, and a close to minimum overall rms error for a, b, c clustering (see Fig. 7 and Table IV).

tical densities in this region could not be digitized to good accuracy with our film digitizer. A review of Fig. 10(c) also shows that the optical density ranges within the breast are about as variable as those outside the breast for the mammograms in this cluster. Some of this variability can be attributed to differences in breast thickness and composition in the

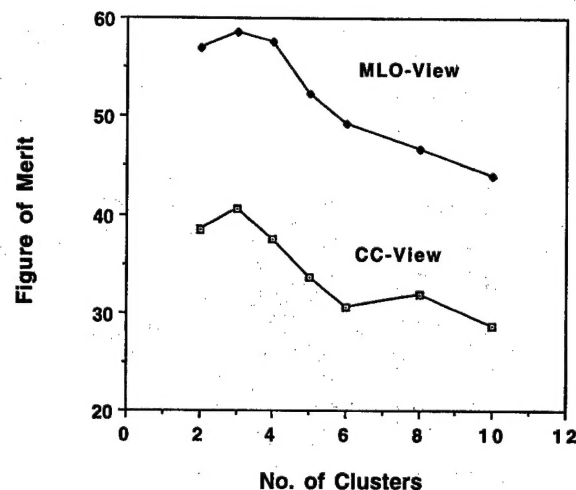


FIG. 7. Plots of clustering figure of merit as a function of number of clusters for the CC- and MLO-views. Both exhibit maximum figure of merits at about three clusters.

regions and some can be attributed to variations in phototimer response, technique (kVp), and film processor conditions.

It is possible that up to three filters of different degrees of equalization will be necessary for the dense, mixed dense and fatty, and fatty breasts or for the thick, medium, and thin breasts in the same breast shape class. We plan to conduct further studies to determine the acceptable range of variation in the primary exposure profiles for each filter subclass. Once the filter subclass criteria are set and the breast images are grouped into the subclasses, the average primary exposure profile of the breast images in a given filter subclass will be

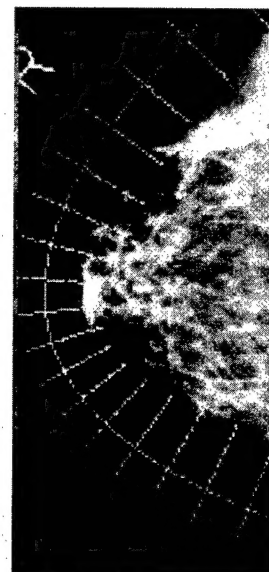


FIG. 8. Example showing overlay of "filter" contour and normals to that contour on one of the mammograms that is classified to belong to the filter shape. The mammogram was histogram equalized using NIH Image to better visualize the breast tissue out to the periphery. The rms distance error to the average "filter" shape is 3.19 mm for this case.

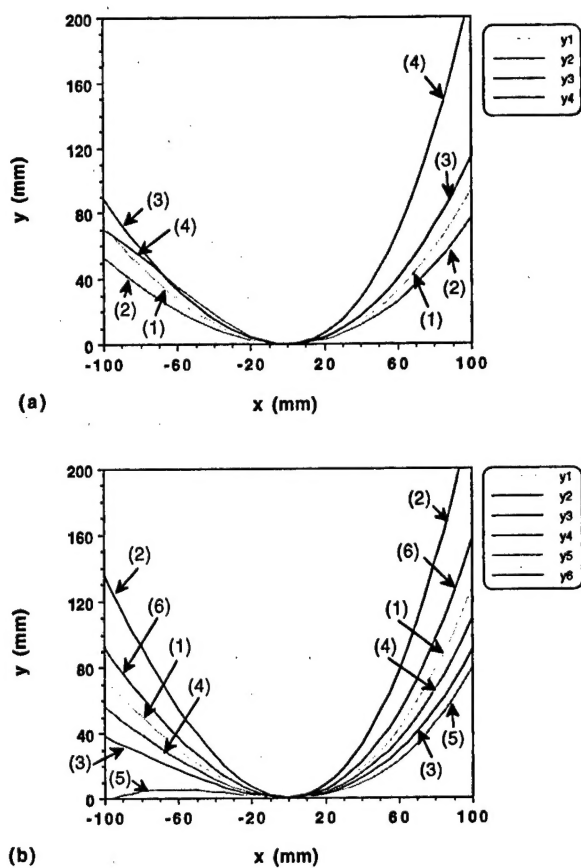


FIG. 9. Examples of "filter" shapes. (a) represents the "filter" shapes derived when the 470 CC-view borders were clustered into 4 groups using the $y = ax^2 + bx^3$ fitting equation. (b) represents the "filter" shapes derived when the 484 MLO-view borders were clustered into six groups using the $y = ax^2 + bx^3$ fitting equation. The number of borders that are classified as being the same shape as the filters in (a) are: 235 for filter #1, 93 for filter #2, 133 for filter #3, and 9 for filter #4. The number of borders that are classified as being the same shape as the filters in (b) are 129 for filter #1, 3 for filter #2, 109 for filter #3, 179 for filter #4, 18 for filter #5, and 46 for filter #6.

estimated by averaging the primary exposure profiles obtained from the individual mammograms in that subclass. The thickness profile of a filter for this subclass can then be derived for a given filter material.

The significance of this study is that, using a large data base of about 500 mammograms in each view, the results support our hypothesis that a small number of pre-fabricated filters will be sufficient to allow selection of a nearly patient-specific filter for each breast being examined. This is the basis of our approach to exposure equalization in mammographic imaging. With this technique, the dynamic range of the x-ray intensities incident on the recording system will be reduced and the entire image can be recorded in the high contrast region of the film. The improved image quality can be achieved without additional radiation dose to the patient. Furthermore, a very high-contrast mammographic technique may be developed in combination with exposure equalization to further improve the signal-to-noise ratio (SNR) of the subtle lesions in the entire breast. We expect that the optimized technique will significantly improve the detectability

of cancers in mixed and dense breasts and increase the efficacy of mammography as a screening and diagnostic tool for breast cancers.

In this work, we assumed that an rms fitting error between the filter contour and a particular breast border of 2 or 3 mm would be acceptable. We based this assumption on the fact that the filter will be smoothly shaped in the thickness dimension as well, which should result in a smooth exposure gradient rather than a step function. Therefore, small gaps between the breast and filter borders should be smoothed out in exposure space.

Mismatches between the filter exposure compensation profiles and the breast attenuation profiles can in practice result in artifacts. For example, if a portion of the filter extends too far toward the inside of the breast, the exposure in this region will be reduced too much, resulting in a light (low optical density) area in the mammogram. Such overcompensation is likely to occur in the MLO-view in the pectoral region where the filters, in general, do not match the breast shapes as well. The filters may have to be designed to have more gradual compensation in these regions to reduce artifacts. To better understand the potential for artifact production and the acceptable rms fitting errors, we are performing a simulation study in which exposure profiles generated in the present study are employed to construct simulated filters which are then applied to images belonging to particular compressed breast shape classes. The results of that study will be presented in a future publication.

Finally, it should be mentioned that our plans for the eventual implementation of the equalization technique do not require the use of a pre-exposure x-ray mammogram of the patient for filter selection. Rather, the filter will be selected based on the measured thickness of the patient's compressed breast, the breast contour as determined from a visible light image of the compressed breast recorded by a TV camera that is interfaced to a computer, and the clustering results gained from a large database of digitized mammograms with corresponding compressed breast thickness information as described in this study. Fabrication of individual filters for a functional system could be accomplished with either a computerized milling machine or stereolithography. Plastics doped with metals such as aluminum and copper might be employed as the filter material in either case to reduce the required filter thickness. The filters would be automatically positioned by a microprocessor controlled stage that translates and rotates the appropriate filter to a location such that the projected filter exposure profile matches the compressed breast border derived from the TV camera image. The filter positioner would be located close to the x-ray tube to minimize x-ray scatter to the breast and minimize artifact production. The individual filters could be placed in the positioner manually, or an automated filter wheel could be developed. Lastly, the entire filter selection/positioning process should take place in only a few seconds to minimize patient discomfort from any additional time the breast must remain compressed.

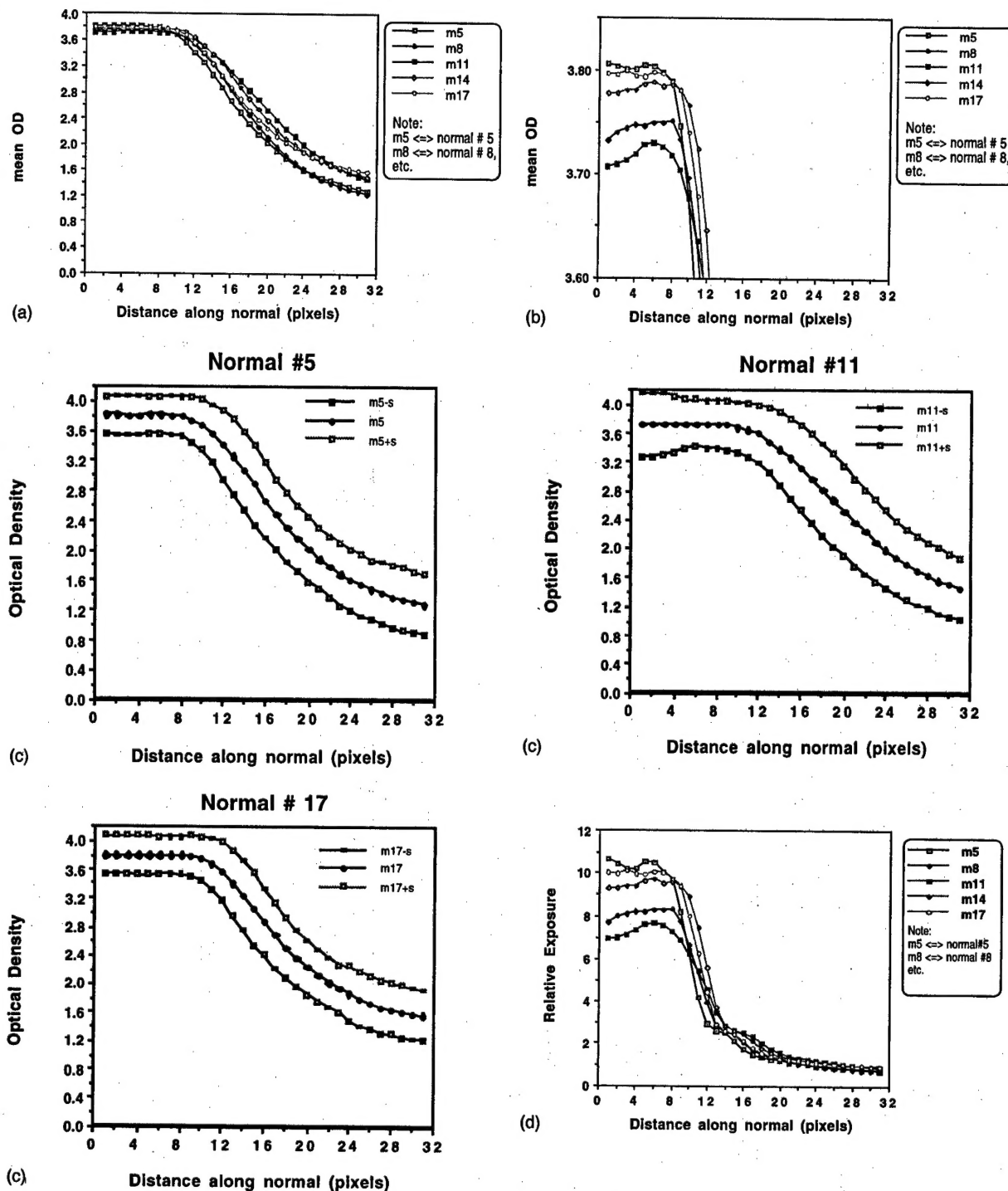


FIG. 10. (a) Mean optical density as a function of position along normals to the filter when the filter is aligned with the automatically detected borders in mammograms classified to belong to the filter shape. For the particular case shown, 231 CC-view borders were classified to match the filter. Pixel #11 along each normal corresponds with the filter edge. Pixels less than 11 are outside the breast, and those greater than 11 are inside the breast. Normal #11 is the middle normal (for a symmetric breast, it is closest to the nipple position). (b) Magnified view showing the details of the high optical density region in plot (a). (c) Mean optical density ± 1 standard deviation for selected normals. (d) Mean exposures corresponding to the optical densities in (a).

ACKNOWLEDGMENT

This work was supported in part by Grant No. DAMD 17-94-J-4292 from the USAMRMC.

^aCorresponding author: Mitchell M. Goodsitt, Ph.D., University of Michigan Hospitals, Department of Radiology, Room B1F510C, 1500 E. Medi-

cal Center Drive, Ann Arbor, MI 48109-0030. Electronic-mail: goodsitt@umich.edu

^bPresent address: Vanstar Corp., 201 Hanfen Ct. Suite 119, Wood Dale, IL 60191.

^cPresent address: Industrial Electronics Lab, GE Corporate R&D, Schenectady, NY 12301.

^dPresent address: Health Physics Office, Walter Reed Army Medical Cen-

ter, Building 41, Rm. 38, 6825 16th St. NW, Washington DC 20307-5001.

¹E. A. Sickles, "Mammographic features of "early" breast cancer," *Am. J. Roentgenol.* **143**, 461-464 (1984).

²E. A. Sickles, "Mammographic features of 300 consecutive nonpalpable breast cancers," *Am. J. Roentgenol.* **146**, 661-663 (1986).

³W. W. Logan and J. A. Janus, "Screen/film mammography," in *Breast Cancer Detection: Mammography and Other Methods in Breast Imaging*, 2nd ed., edited by L. W. Bassett and R. H. Gold (Grune & Stratton, New York, 1987).

⁴R. M. Nishikawa, G. E. Mawdsley, A. Fenster, and M. J. Yaffe, "Scanned-projection digital mammography," *Med. Phys.* **14**, 717-727 (1987).

⁵R. M. Nishikawa and M. J. Yaffe, "An investigation of digital mammographic imaging," *Proc. SPIE* **419**, 192-200 (1983).

⁶P. C. Bunch, K. E. Huff, and R. Van Metter, "Analysis of the detective quantum efficiency of a radiographic screen/film system," *J. Opt. Soc. Am. A* **4**, 902-909 (1987).

⁷H. R. Blackwell, "Contrast thresholds of the human eye," *J. Opt. Soc. Am.* **36**, 624-643 (1946).

⁸B. Baxter, H. Ravinda, and R. A. Normann, "Changes in lesion detectability caused by light adaptation in retinal photo-receptors," *Invest. Radiol.* **17**, 394-401 (1982).

⁹H. L. Snyder, "Chapter 3: The Visual System: Capabilities and Limitations," in *Flat-Panel Display and CRTs*, edited by L. E. Tannas, Jr. (Van Nostrand Reinhold, New York, 1985).

¹⁰L. D'Agincourt, "Technique is everything when breast is dense," *Diagnostic Imaging*, Sept., 57-61 (1993).

¹¹K. L. Lam and H.-P. Chan, "Development of x-ray beam equalization technique in mammography," *Radiology* **169**(P), 338 (1988).

¹²K. L. Lam and H.-P. Chan, "Exposure equalization techniques in mammography," *Invest. Radiol.* **24**, 154-157 (1989).

¹³K. L. Lam and H.-P. Chan, "Effects of x-ray beam equalization on mammographic imaging," *Med. Phys.* **17**, 242-249 (1990).

¹⁴G. Panayiotakis, H. Likaki, Z. Kolitsi, and J. Dimopoulos, "An anatomical filter for exposure equalization in mammography," *Eur. J. Radiol.* **15**, 15-17 (1992).

¹⁵J. M. Sabol, I. C. Soutar, and D. B. Plewes, "Mammographic scanning equalization radiography," *Med. Phys.* **20**, 1505-1515 (1993).

¹⁶J. W. Oestmann, B. Stoel, H. Schrijvershof, J. Vrooman, and L. J. Schultze Kool, "Scanning equalization mammography: Preliminary evaluation," *Radiographics* **14**, 123-128 (1994).

¹⁷J. M. Sabol, I. C. Soutar, and D. B. Plewes, "Practical application of a scan-rotate equalization geometry to mammography," *Med. Phys.* **23**, 1987-1996 (1996).

¹⁸A. R. Morton, H. P. Chan, and M. M. Goodsitt, "Automated model-guided breast segmentation algorithm," *Med. Phys.* **23**, 1107-1108 (1996).

¹⁹M. M. Goodsitt, H.-P. Chan, B. Liu, S. Guru, and R. Morton, "Compressed breast shape classification for the design of mammography equalization filters," *Med. Phys.* **23**, 1108 (1996).

²⁰M. R. Andenberg, *Cluster Analysis for Applications* (Academic, New York, 1973).